Rational construction of a library of M_{29} nanoclusters from monometallic to tetrametallic

Xi Kang[a], Xiao Wei[a], Shan Jin[a], Qianqin Yuan[a], Xinqi Luan[b], Yong Pei[b], Shuxin Wang[a,*], Manzhou Zhu[a,*] and Rongchao Jin[c,*]

Affiliations

[a] Department of Chemistry and Centre for Atomic Engineering of Advanced Materials, Anhui Province Key Laboratory of Chemistry for Inorganic/Organic Hybrid Functionalized Materials, Anhui University, Hefei, Anhui 230601, China.

[b] Department of Chemistry, Key Laboratory of Environmentally Friendly Chemistry and Applications of Ministry of Education, Xiangtan University, Xiangtan, Hunan 411105, China.

[c] Department of Chemistry, Carnegie Mellon University, Pittsburgh, PA 15213, USA.

E-mail

Shuxin Wang
Email: ixing@ahu.edu.cn
Manzhou Zhu
Email: zmz@ahu.edu.cn
Rongchao Jin
Email: rongchao@andrew.cmu.edu

This PDF file includes:

Materials and Methods
Figs. S1 to S53
Tables S1 to S4

Methods

Materials. All chemicals including silver nitrate ($AgNO_3$, 99.9%, metal basis), tetrachloroauric (III) acid ($HAuCl_4 \bullet 4H_2O$, 99.9%, metal basis), cuprous chloride (CuCl, 99.9%, metal basis), palladium acetate ($Pd(OAc)_2$, 99.9% metals basis), hexachloroplatinic (IV) acid ($H_2PtCl_6 \cdot 6H_2O$, 99.9% metals basis), triphenylphosphine (PPh_3, 99%), 1-adamantanethiol (Adm-SH, $C_{10}H_{15}SH$, 99%), methyl sulfide ($S(CH_3)_2$, 99%), sodium borohydride ($NaBH_4$, 99.9%), hydrogen peroxide solution (H_2O_2, 30 wt. % in H_2O, GR grade), methylene chloride (CH_2Cl_2, HPLC grade), methanol (CH_3OH, HPLC), ethanol (CH_3CH_2OH, HPLC), acetic ether ($CH_3COOC_2H_5$, HPLC), acetonitrile (CH_3CN, HPLC grade) are purchased from Sigma-Aldrich and used without further purification. Pure water is purchased from Wahaha Co. Ltd. All glassware are thoroughly cleaned with aqua regia (HCl: HNO_3 = 3:1 vol.), rinsed with copious pure water, and then dried in an oven prior to use.

Synthesis of $Au^I(PPh_3)Cl$ complex. $HAuCl_4 \bullet 4H_2O$ (0.42 g, 1 mmol) was dissolved in CH_3OH (20 mL). $(CH_3)_2S$ (380 μL, 5 mmol) was added under vigorous stirring (~1200 rpm) and the stirring was continued for 30 min. The precipitate was then collected and further dissolved in 30 mL CH_2Cl_2. After that, PPh_3 (0.29 g, 1.1 mmol) was dissolved in CH_2Cl_2 (10 mL) and added to the first solution in a dropwise manner under vigorous stirring (~1200 rpm) and the stirring was continued for 15 min. The resulting mixture was then filtered. The filtrate was slowly rotavaporated under vacuum. The final product ($Au^I(PPh_3)Cl$) was directly used in the next step.

Synthesis of $Ag^I(PPh_3)NO_3$ or $Cu^I(PPh_3)_2Cl$ complex. $AgNO_3$ (0.17 g, 1 mmol) or CuCl (0.1 g, 1 mmol) was dissolved in CH_3CN (5 mL). PPh_3 (0.29 g, 1.1 mmol for the Ag^I complex and 0.58 g, 2.2 mmol for the Cu^I complex) was dissolved in CH_3CN (10 mL) and added to the first solution in a dropwise manner under vigorous stirring (~1200 rpm) and the stirring was continued for 15 min. The resulting mixture was then filtered. The filtrate was slowly rotavaporated under vacuum. The final product ($Ag^I(PPh_3)NO_3$ or $Cu^I(PPh_3)_2Cl$) was directly used in the next step.

Synthesis of mono-metallic $[Ag_{29}(S\text{-}Adm)_{18}(PPh_3)_4]^{3+}$ nanocluster. For the nanocluster synthesis, $AgNO_3$ (30 mg, 0.18 mmol) was dissolved in CH_3OH (5 mL) and $CH_3COOC_2H_5$ (35 mL) with sonication. The solution was vigorously stirred (~1200 rpm) with magnetic stirring for 15 min. Then, Adm-SH (0.1 g) and PPh_3 (0.1 g) were added and the reaction was vigorously stirred (~1200 rpm) for another 90 min. After that, $NaBH_4$ (1 mL) aqueous solution (20 mg mL^{-1}) was added quickly to the above mixture. The reaction was allowed to proceed for 36 h under a N_2 atmosphere. After that, the aqueous layer was removed, and the mixture in the organic phase was rotavaporated under vacuum. Then approximately 15*3 mL of CH_3OH was used to wash the synthesized nanoclusters. The precipitate was dissolved in CH_2Cl_2, which produced the $[Ag_{29}(S\text{-}Adm)_{18}(PPh_3)_4]^{3+}$ nanocluster. The yield is 16% based on the Ag element (calculated from the $AgNO_3$) for synthesizing the $[Ag_{29}(S\text{-}Adm)_{18}(PPh_3)_4]^{3+}$ nanocluster.

Synthesis of bi-metallic $[Au_1Ag_{28}(S\text{-}Adm)_{18}(PPh_3)_4]^{3+}$ nanocluster. Specifically, the metal source for synthesizing $[Ag_{29}(S\text{-}Adm)_{18}(PPh_3)_4]^{3+}$ nanocluster (*i.e.*, $AgNO_3$, 0.18 mmol) was altered to Ag/Au mixture ($AgNO_3/Au^I(PPh_3)Cl$ = 0.172/0.008 mmol in the $[Au_1Ag_{28}(S\text{-}Adm)_{18}(PPh_3)_4]^{3+}$ synthesis) and the other conditions were not changed, then the $[Au_1Ag_{28}(S\text{-}Adm)_{18}(PPh_3)_4]^{3+}$

nanocluster was obtained. The yield is 25% based on the Ag element (calculated from the $AgNO_3$) for synthesizing the $[Au_1Ag_{28}(S\text{-}Adm)_{18}(PPh_3)_4]^{3+}$ nanocluster. It should be noted that the small amount of $Au^I(PPh_3)Cl$ in the Ag/Au mixture (~ 20/1) is important for synthesizing the $[Au_1Ag_{28}(S\text{-}Adm)_{18}(PPh_3)_4]^{3+}$ nanocluster in mono-dispersity.

Synthesis of bi-metallic $[M_1Ag_{28}(S\text{-}Adm)_{18}(PPh_3)_4]^{2+}$ (M=Pt/Pd) nanoclusters. Specifically, the metal source for synthesizing $[Ag_{29}(S\text{-}Adm)_{18}(PPh_3)_4]^{3+}$ nanocluster (*i.e.*, $AgNO_3$, 0.18 mmol) was altered to Ag/Pt or Ag/Pd mixture ($AgNO_3/H_2PtCl_6{\cdot}6H_2O$ = 0.17/0.01 mmol in the $[Pt_1Ag_{28}(S\text{-}Adm)_{18}(PPh_3)_4]^{2+}$ synthesis or $AgNO_3/Pd(OAc)_2$ = 0.17/0.01 mmol in the $[Pd_1Ag_{28}(S\text{-}Adm)_{18}(PPh_3)_4]^{2+}$ synthesis) and the other conditions were not changed, then the $[M_1Ag_{28}(S\text{-}Adm)_{18}(PPh_3)_4]^{2+}$ (M = Pt/Pd) nanoclusters were obtained. The yields are 45% and 16% based on the Ag element (calculated from the $AgNO_3$) for synthesizing the $[Pt_1Ag_{28}(S\text{-}Adm)_{18}(PPh_3)_4]^{2+}$ and $[Pd_1Ag_{28}(S\text{-}Adm)_{18}(PPh_3)_4]^{2+}$ nanoclusters, respectively.

Synthesis of tri-metallic $[Pt_1Ag_{12+x}Cu_{16-x}(S\text{-}Adm)_{18}(PPh_3)_4]^{2+}$ (x = 0-4) nanoclusters. Specifically, the metal source for synthesizing $[Ag_{29}(S\text{-}Adm)_{18}(PPh_3)_4]^{3+}$ nanocluster (*i.e.*, $AgNO_3$, 0.18 mmol) was altered to Ag/Cu/Pt mixture ($AgNO_3/Cu^I(PPh_3)_2Cl/H_2PtCl_6{\cdot}6H_2O$ = 0.1/0.07/0.01 mmol in the $[Pt_1Ag_{12+x}Cu_{16-x}(S\text{-}Adm)_{18}(PPh_3)_4]^{2+}$ synthesis) and the other conditions were not changed, then the $[Pt_1Ag_{12+x}Cu_{16-x}(S\text{-}Adm)_{18}(PPh_3)_4]^{2+}$ nanoclusters were obtained. The yield is 15% based on the Ag element (calculated from the $AgNO_3$) for synthesizing the $[Pt_1Ag_{12+x}Cu_{16-x}(S\text{-}Adm)_{18}(PPh_3)_4]^{2+}$ nanoclusters.

Synthesis of tri-metallic $[Pt_1Ag_{12}Cu_{16}(S\text{-}Adm)_{18}(PPh_3)_4]^{2+}$ and $[Pt_1Ag_{16}Cu_{12}(S\text{-}Adm)_{18}(PPh_3)_4]^{2+}$ nanoclusters. A target metal-exchange method was exploited to "focus" the poly-dispersed $[Pt_1Ag_{12+x}Cu_{16-x}(S\text{-}Adm)_{18}(PPh_3)_4]^{2+}$ (x = 0-4) nanoclusters into the $[Pt_1Ag_{12}Cu_{16}(S\text{-}Adm)_{18}(PPh_3)_4]^{2+}$ or $[Pt_1Ag_{16}Cu_{12}(S\text{-}Adm)_{18}(PPh_3)_4]^{2+}$. Specifically, 0.1 mmol $[Pt_1Ag_{12+x}Cu_{16-x}(S\text{-}Adm)_{18}(PPh_3)_4]^{2+}$ was dissolved in 20 mL CH_2Cl_2. 1 mmol $Cu^I(PPh_3)_2Cl$ was added to the above solution and the solution was further vigorously stirred (~1200 rpm) for 30 min. The organic phase was rotavaporated under vacuum and washed several times with CH_3OH. The precipitate was dissolved in CH_2Cl_2, which produced pure $[Pt_1Ag_{12}Cu_{16}(S\text{-}Adm)_{18}(PPh_3)_4]^{2+}$. The yield is 80% based on the $[Pt_1Ag_{12+x}Cu_{16-x}(S\text{-}Adm)_{18}(PPh_3)_4]^{2+}$ nanoclusters for synthesizing the $[Pt_1Ag_{12}Cu_{16}(S\text{-}Adm)_{18}(PPh_3)_4]^{2+}$ nanocluster. Changing the $Cu^I(PPh_3)Cl$ into the $Ag^I(PPh_3)NO_3$ generated pure $[Pt_1Ag_{16}Cu_{12}(S\text{-}Adm)_{18}(PPh_3)_4]^{2+}$ with 70% yield.

Synthesis of tri-metallic $[Pd_1Ag_{12+x}Cu_{16-x}(S\text{-}Adm)_{18}(PPh_3)_4]^{2+}$ (x = 0-4), $[Pd_1Ag_{12}Cu_{16}(S\text{-}Adm)_{18}(PPh_3)_4]^{2+}$, and $[Pd_1Ag_{16}Cu_{12}(S\text{-}Adm)_{18}(PPh_3)_4]^{2+}$ nanoclusters. The synthesis of Pd-centered tri-metallic nanoclusters are the same as the synthetic procedures of the Pt-centered tri-metallic nanoclusters, just by altering the $H_2PtCl_6{\cdot}6H_2O$ source to $Pd(OAc)_2$.

Synthesis of tri-metallic $[Au_1Ag_{12+x}Cu_{16-x}(S\text{-}Adm)_{18}(PPh_3)_4]^{3+}$ (x = 0-4) nanoclusters. Specifically, the metal source for synthesizing $[Ag_{29}(S\text{-}Adm)_{18}(PPh_3)_4]^{3+}$ nanocluster (*i.e.*, $AgNO_3$, 0.18 mmol) was altered to Ag/Cu/Au mixture ($AgNO_3/Cu^I(PPh_3)_2Cl/Au^I(PPh_3)Cl$ = 0.1/0.075/0.005 mmol in the $[Au_1Ag_{12+x}Cu_{16-x}(S\text{-}Adm)_{18}(PPh_3)_4]^{2+}$ synthesis) and the other conditions were not changed, then the $[Au_1Ag_{12+x}Cu_{16-x}(S\text{-}Adm)_{18}(PPh_3)_4]^{2+}$ nanoclusters were obtained. The yield is 25% based on

the Ag element (calculated from the $AgNO_3$) for synthesizing the $[Au_1Ag_{12+x}Cu_{16-x}(S\text{-}Adm)_{18}(PPh_3)_4]^{3+}$ nanoclusters. It should be noted that the small amount of $Au^I(PPh_3)Cl$ in the Ag/Cu/Au (~10/10/1) mixture is important for synthesizing the $[Au_1Ag_{12+x}Cu_{16-x}(S\text{-}Adm)_{18}(PPh_3)_4]^{3+}$ nanocluster in mono-dispersity.

Synthesis of tri-metallic $[Au_1Ag_{12+x}Cu_{16-x}(S\text{-}Adm)_{18}(PPh_3)_4]^{3+}$ (x = 0-4), $[Au_1Ag_{12}Cu_{16}(S\text{-}Adm)_{18}(PPh_3)_4]^{3+}$, and $[Au_1Ag_{16}Cu_{12}(S\text{-}Adm)_{18}(PPh_3)_4]^{3+}$ nanoclusters. The syntheses of Au-centered tri-metallic nanoclusters were the same as the synthetic procedures in the synthesis of Pt-centered tri-metallic nanoclusters, just by altering the $[Pt_1Ag_{12+x}Cu_{16-x}(S\text{-}Adm)_{18}(PPh_3)_4]^{2+}$ precursor to the $[Au_1Ag_{12+x}Cu_{16-x}(S\text{-}Adm)_{18}(PPh_3)_4]^{3+}$ precursor.

Synthesis of tetra-metallic $[Pt_1Ag_{12}Cu_{16-x}Au_x(S\text{-}Adm)_{18}(PPh_3)_4]^{2+}$ (x = 0-4) nanoclusters. A target metal-exchange method was exploited to alloy the tri-metallic $[Pt_1Ag_{12}Cu_{16}(S\text{-}Adm)_{18}(PPh_3)_4]^{2+}$ nanocluster into the tetra-metallic $[Pt_1Ag_{12}Cu_{16-x}Au_x(S\text{-}Adm)_{18}(PPh_3)_4]^{2+}$ (x = 0-4) nanoclusters. Specifically, 0.1 mmol $[Pt_1Ag_{12}Cu_{16}(S\text{-}Adm)_{18}(PPh_3)_4]^{2+}$ was dissolved in 20 mL CH_2Cl_2. 0.5 mmol $Au^I(PPh_3)Cl$ was added to the above solution and the solution was further vigorously stirred (~1200 rpm) for 60 min. The organic phase was rotavaporated under vacuum. The precipitate was dissolved in CH_2Cl_2, which produced the tetra-metallic $[Pt_1Ag_{12}Cu_{16-x}Au_x(S\text{-}Adm)_{18}(PPh_3)_4]^{2+}$ nanocluster. The yield is 85% based on the $[Pt_1Ag_{12}Cu_{16}(S\text{-}Adm)_{18}(PPh_3)_4]^{2+}$ for synthesizing the $[Pt_1Ag_{12}Cu_{16-x}Au_x(S\text{-}Adm)_{18}(PPh_3)_4]^{2+}$ nanocluster.

Synthesis of tetra-metallic $[Pt_1Ag_{12}Cu_{12}Au_4(S\text{-}Adm)_{18}(PPh_3)_4]^{2+}$ nanocluster. The forced metal-exchange method was exploited to alloy the poly-dispersed $[Pt_1Ag_{12}Cu_{16-x}Au_x(S\text{-}Adm)_{18}(PPh_3)_4]^{2+}$ (x = 0-4) nanoclusters into the mono-dispersed $[Pt_1Ag_{12}Cu_{12}Au_4(S\text{-}Adm)_{18}(PPh_3)_4]^{2+}$ nanocluster. Specifically, 0.1 mmol $[Pt_1Ag_{12}Cu_{16-x}Au_x(S\text{-}Adm)_{18}(PPh_3)_4]^{2+}$ was dissolved in 20 mL CH_2Cl_2. 200 µL H_2O_2 was added and the solution was further vigorously stirred (~1200 rpm) for 3 min. Then 0.5 mmol $Au^I(PPh_3)Cl$ was added to the above solution and further vigorously stirred for 30 min. The H_2O_2@$Au^I(PPh_3)Cl$ addition was repeated 3 times to eliminate the Cu^I coordination completely. The organic phase was then precipitated with a large amount of CH_3OH. Finally, the precipitate was dissolved in CH_2Cl_2, which produced the mono-dispersed $[Pt_1Ag_{12}Cu_{16}Au_4(S\text{-}Adm)_{18}(PPh_3)_4]^{2+}$ nanocluster. The yield is 20% based on the $[Pt_1Ag_{12}Cu_{16-x}Au_x(S\text{-}Adm)_{18}(PPh_3)_4]^{2+}$ for synthesizing the $[Pt_1Ag_{12}Cu_{16}Au_4(S\text{-}Adm)_{18}(PPh_3)_4]^{2+}$ nanocluster.

Synthesis of tetra-metallic $[Pd_1Ag_{12}Cu_{16-x}Au_x(S\text{-}Adm)_{18}(PPh_3)_4]^{2+}$ (x = 0-4) and $[Pd_1Ag_{12}Cu_{12}Au_4(S\text{-}Adm)_{18}(PPh_3)_4]^{2+}$ nanoclusters. The syntheses of Pd-centered tetra-metallic nanoclusters are the same as the synthetic procedures in the synthesis of the Pt-centered tetra-metallic nanoclusters, just by altering the $[Pt_1Ag_{12}Cu_{16}(S\text{-}Adm)_{18}(PPh_3)_4]^{2+}$ precursor to the $[Pd_1Ag_{12}Cu_{16}(S\text{-}Adm)_{18}(PPh_3)_4]^{2+}$.

Following the aforementioned target metal-exchange and forced metal-exchange methods to control the four vertex metal atoms, other 9 alloy nanoclusters with mono-dispersity were obtained, including $Ag_{25}Au_4$, $Ag_{25}Cu_4$, $Ag_{24}Au_5$, $Au_1Ag_{24}Cu_4$, $Au_5Ag_{12}Cu_{12}$, $Pt_1Au_4Ag_{24}$, $Pt_1Cu_4Ag_{24}$, $Pd_1Au_4Ag_{24}$ and $Pd_1Cu_4Ag_{24}$ nanoclusters.

Crystallization of $Au_1Ag_{28}(S\text{-}Adm)_{18}(PPh_3)_4$ and $Pt_1Ag_{12}Cu_{16}(S\text{-}Adm)_{18}(PPh_3)_4$ nanoclusters. Single crystals of $Au_1Ag_{28}(S\text{-}Adm)_{18}(PPh_3)_4$ and $Pt_1Ag_{12}Cu_{16}(S\text{-}Adm)_{18}(PPh_3)_4$ nanoclusters were grown at room temperature for 7 days in CH_2Cl_2/CH_3OH. This step was repeated for 3 times to obtain high quality single crystals. Then, red crystals were collected and the structures of $Au_1Ag_{28}(S\text{-}Adm)_{18}(PPh_3)_4$ and $Pt_1Ag_{12}Cu_{16}(S\text{-}Adm)_{18}(PPh_3)_4$ nanoclusters were determined by X-ray crystallography.

Characterizations. All UV-vis absorption spectra of nanoclusters dissolved in CH_2Cl_2 were recorded using an Agilent 8453 diode array spectrometer, whose background correction was made using a CH_2Cl_2 blank. Nanocluster samples were dissolved in CH_2Cl_2 to make dilute solutions, followed by spectral measurement (1 cm path length quartz cuvette).

Electrospray ionization time-of-flight mass spectrometry (ESI-TOF-MS) measurement was performed by MicrOTOF-QIII high-resolution mass spectrometer. The sample was directly infused into the chamber at 5 μL/min. To prepare the ESI sample, nanoclusters were dissolved in CH_2Cl_2 (1 mg/mL) and diluted (*v*/*v*=1:2) by CH_3OH. Mass spectra of nanoclusters are measured in the positive mode.

PL spectra were measured on an FL-4500 spectrofluorometer with the same optical density (OD) of ~0.05. In these experiments, the nanocluster solutions were prepared in CH_2Cl_2 at a concentration of less than 1 mg mL^{-1}.

Quantum yields (QYs) were measured with dilute solutions of nanoclusters on a HORIBA FluoroMax-4P.

X-ray photoelectron spectroscopy (XPS) measurement was performed on a Thermo ESCALAB 250, configured with a monochromated AlKα (1486.8 eV) 150W X-ray source, 0.5 mm circular spot size, a flood gun to counter charging effects, and the analysis chamber base pressure lower than $1x10^{-9}$ mbar, data were collected with FAT=20 eV.

Element analysis (EA) was performed on Vario EL cube. 3 mg of each sample was used in the experiment.

Inductively coupled plasma-atomic emission spectrometry (ICP-AES) measurement was performed on an Atomscan Advantage instrument made by Thormo Jarrell Ash Corporation (USA). The nanoclusters were digested by concentrated nitric acid and the concentration of the nanoclusters were set to 0.5 mg L^{-1} approximately.

^{31}P nuclear magnetic resonance (NMR) spectra were acquired using a Bruker 600 AVANAC III spectrometer equipped with a Bruker BBO multinuclear probe (BrukerBioSpin, Rheinstetten, Germany). To achieve a sufficient signal-to-noise ratio, the ^{31}P NMR spectra were recorded by collecting 1k scans with a recycle delay time of 5s.

X-Ray Crystallography. The data collection for single crystal X-ray diffraction was carried out on a Bruker Smart APEX II CCD diffractometer under liquid nitrogen flow, using graphite-monochromatized Mo Kα radiation (λ = 0.71073 Å). Data reductions and absorption corrections were performed using the SAINT and SADABS programs, respectively.[S1] The electron density was squeezed by platon, and solvent has also been squeezed by platon. Detailed information can be found in the Supplementary Tables S3 and S4. The structure was solved by direct methods and refined with full-matrix least squares on F^2 using the SHELXTL software

package.[S2] All non-hydrogen atoms were refined anisotropically, and all the hydrogen atoms were set in geometrically calculated positions and refined isotropically using a riding model.

Theoretical Methods. The structural optimizations are carried out using the DMol^3 package.[S3,S4] In these calculations, the generalized gradient approximation (GGA) with the Perdew-Burkr-Ernzerhof (PBE) functional.[S5] Moreover, considering the computational accuracy and efficiency, the DND4.4 basis chosen in the structural optimization. The Tkatchenko-Scheffler (TS) method is used for the DFT-D calculations.[S6] The convergence criterion of the geometrical optimization was set to be 1.0×10^{-5} Hartree for energy change, 4.0×10^{-3} Hartree/Å for the gradient, and 5.0×10^{-3} Å for the atom displacement, respectively.

Reference:

[S1] G. M. Sheldrick. SADABS; University of Gottingen: Gottingen, Germany, **1996**.

[S2] D. M. Sheldrick. Crystal structure refinement with SHELXL. *Acta Crystallogr., Sect. C: Struct. Chem.* **2015**, *71*, 3-8.

[S3] B. Delley. From Molecules to Solids with the DMol3 Approach. *J. Chem. Phys.* **2000**, *113*, 7756-7764.

[S4] B. Delley. An All-Electron Numerical Method for Solving the Local Density Functional for Polyatomic Molecules. *J. Chem. Phys.* **1990**, *92*, 508-517.

[S5] J. P. Perdew, K. Burke, M. Ernzerhof. Generalized Gradient Approximation Made Simple. *Phys. Rev. Lett.* **1996**, *77*, 3865-3868.

[S6] J. P. Perdew, V. N. Staroverov, G. E. Scuseria, J. Tao. Climbing the Density Functional Ladder: Nonempirical Meta--Generalized Gradient Approximation Designed for Molecules and Solids. *Phys. Rev. Lett.* **2003**, *91*, 146401.

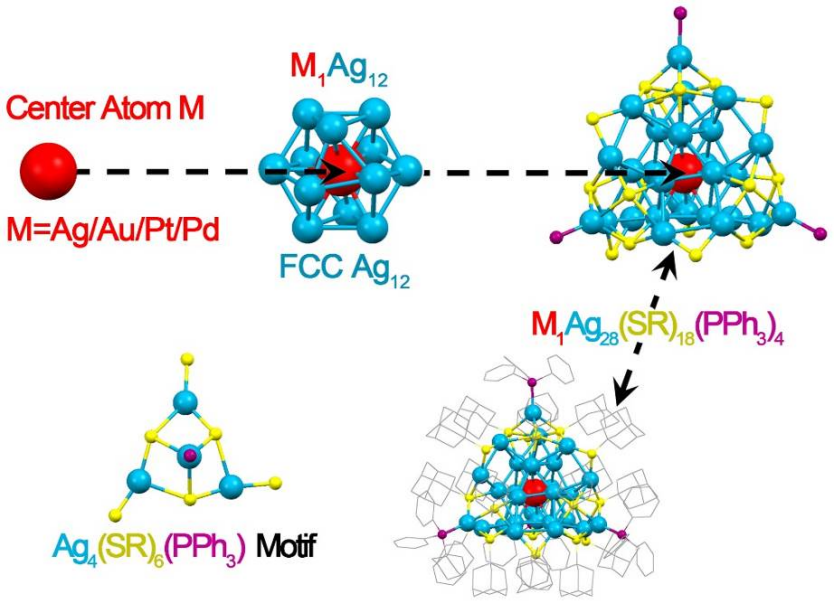

Fig. S1 Structural anatomy of the $M_1Ag_{28}(SR)_{18}(PPh_3)_4$ nanoclusters (where, M = Ag/Au/Pt/Pd, SR = S-Adm). Color codes: red sphere, the center atom M; cerulean sphere, Ag; yellow sphere, S; purple sphere, P; grey sphere, C. For clarity, the hydrogen atoms are not shown.

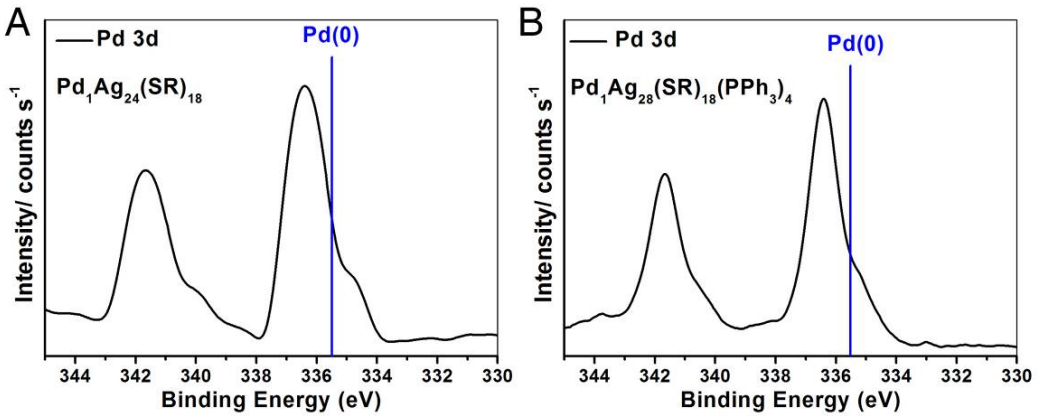

Fig. S2 X-ray photoelectron spectroscopy (XPS) of the Pd 3d in (A) $Pd_1Ag_{24}(SR)_{18}$ or (B) $Pd_1Ag_{28}(SR)_{18}(PPh_3)_4$ nanoclusters.

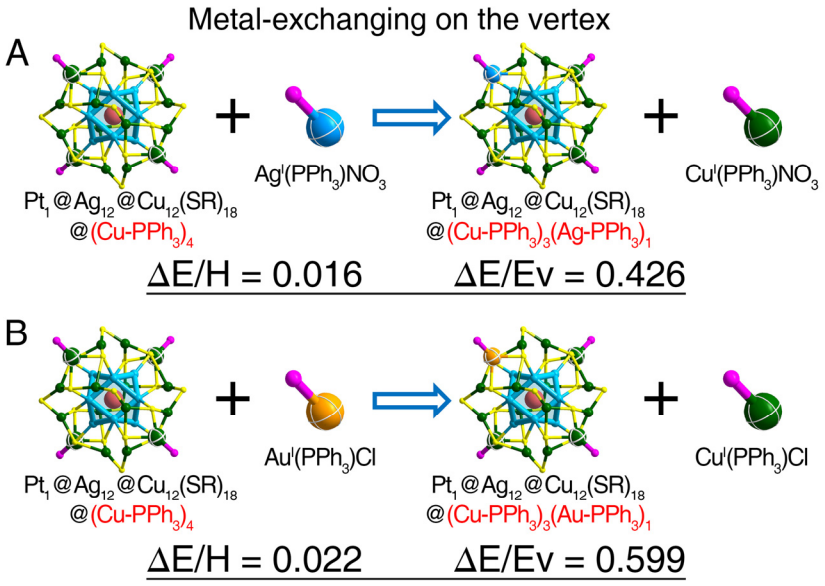

Fig. S3 Required energy by substituting a vertex Cu atom in $Pt_1@Ag_{12}@Cu_{12}(SR)_{18}@(Cu\text{-}PPh_3)_4$ with (A) an Ag heteroatom from $Ag^I(PPh_3)NO_3$, or (B) an Au heteroatom from $Au^I(PPh_3)Cl$. The required energy in Au-doping is much larger than in Ag-doping (0.599 versus 0.426), demonstrating that (i) the Au-doping process is harder than the Ag doping process, and (ii) the $Pt_1@Ag_{12}@Ag_{12}(SR)_{18}@(Cu\text{-}PPh_3)_4$ is more stable than the obtained $Pt_1@Ag_{12}@Ag_{12}(SR)_{18}@(Cu\text{-}PPh_3)_3(Au\text{-}PPh_3)_1$.

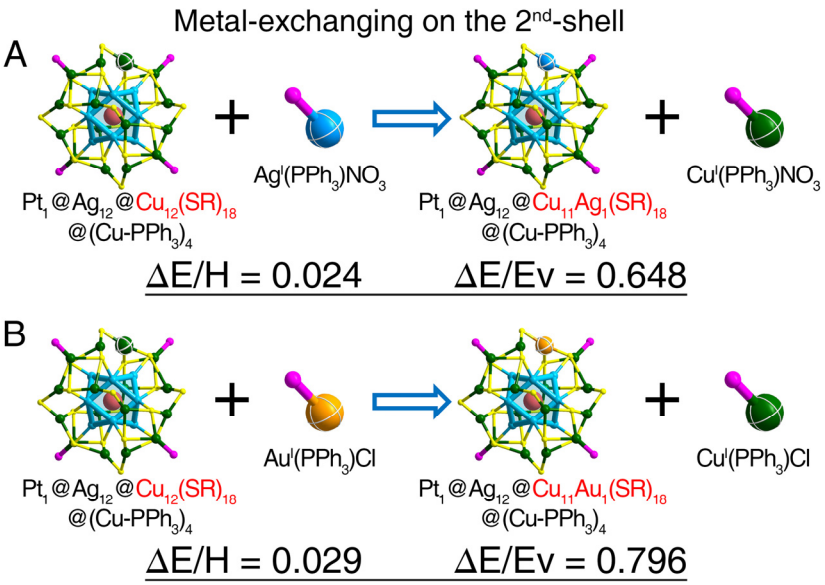

Fig. S4 Required energy by substituting a 2nd-shell Cu atom in $Pt_1@Ag_{12}@Ag_{12}(SR)_{18}@(Cu\text{-}PPh_3)_4$ with (A) an Ag heteroatom from $Ag^I(PPh_3)NO_3$, or (B) an Au heteroatom from $Au^I(PPh_3)Cl$. The required energies is all larger (~30%) than substituting a vertex Cu atom, either for Ag-doping or the Au-doping process. In this context, the metal-exchang location is the vertex, but not the 2nd-shell

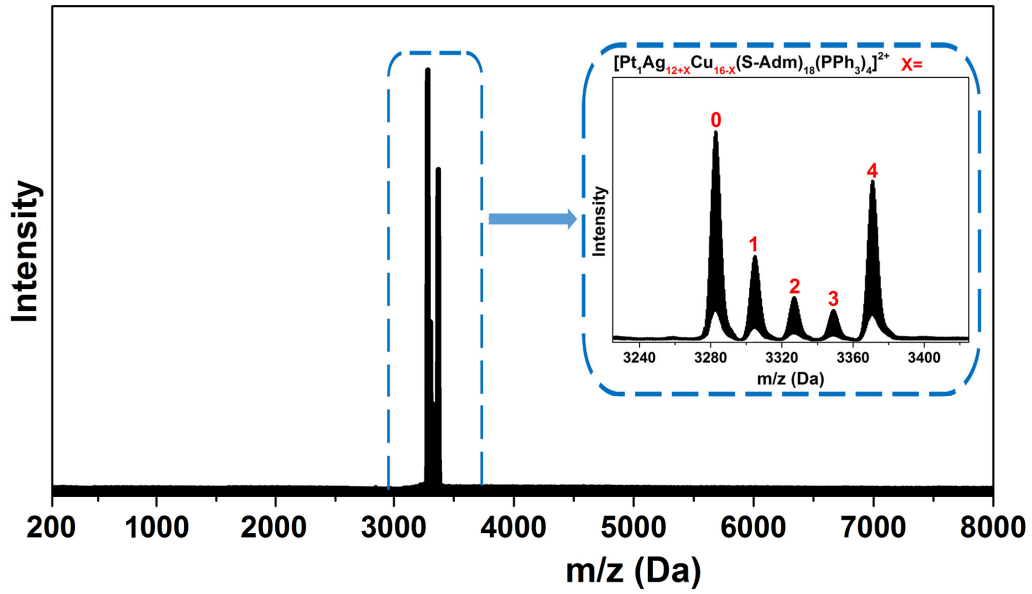

Fig. S5 Expansion of the ESI-MS spectrum in the 200-8000 Da (inset: 3220-3430 Da range) mass range of the $[Pt_1Ag_{12+x}Cu_{16-x}(S\text{-}Adm)_{18}(PPh_3)_4]^{2+}$ (x = 0-4) nanoclusters.

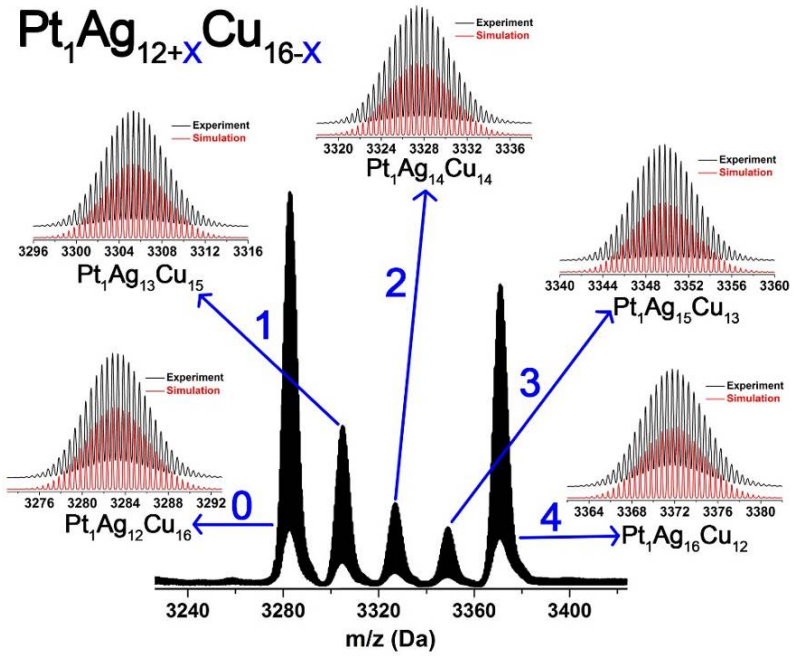

Fig. S6 ESI-MS spectrum in 3230-3430 Da mass range of the $[Pt_1Ag_{12+x}Cu_{16-x}(S\text{-}Adm)_{18}(PPh_3)_4]^{2+}$ (x = 0-4) nanoclusters. Insets: the experimental (black) and simulated (red) isotope patterns of each component in this mixture.

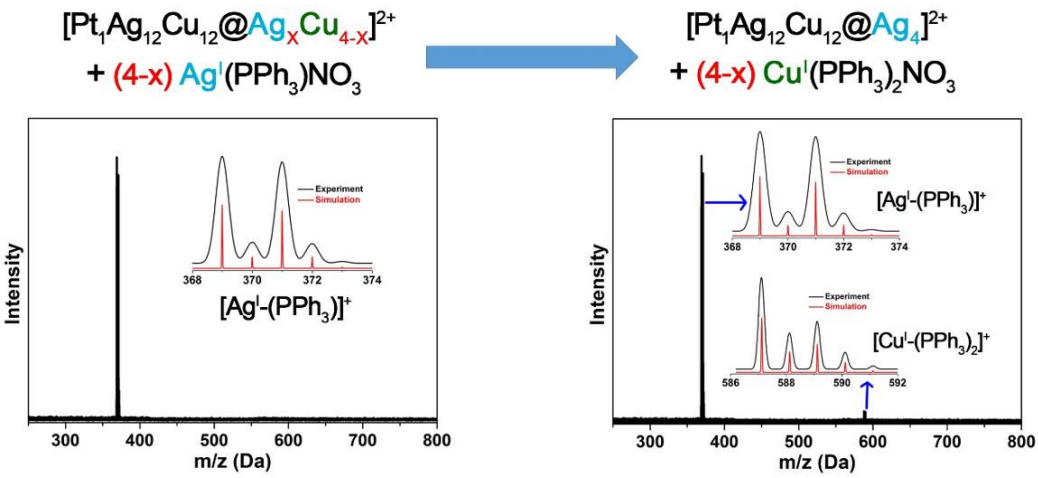

Fig. S7 ESI-MS spectra of $[Ag^{I}\text{-}(PPh_3)]^+$ and the metal-exchanged products (i.e., the mixture of $[Ag^{I}\text{-}(PPh_3)]^+$ and $[Cu^{I}\text{-}(PPh_3)_2]^+$. It should be noted that the $[Cu^{I}\text{-}(PPh_3)_2]^+$ is from the $Pt_1Ag_{12}Cu_{12}@Ag_xCu_{4-x}$ nanoclusters. The reaction equation is: $Pt_1Ag_{12}Cu_{12}@Ag_xCu_{4-x}$ + (4-*x*) $Ag^{I}(PPh_3)NO_3$ → $Pt_1Ag_{12}Cu_{12}@Ag_4$ + (4-*x*) $Cu^{I}(PPh_3)_2NO_3$.

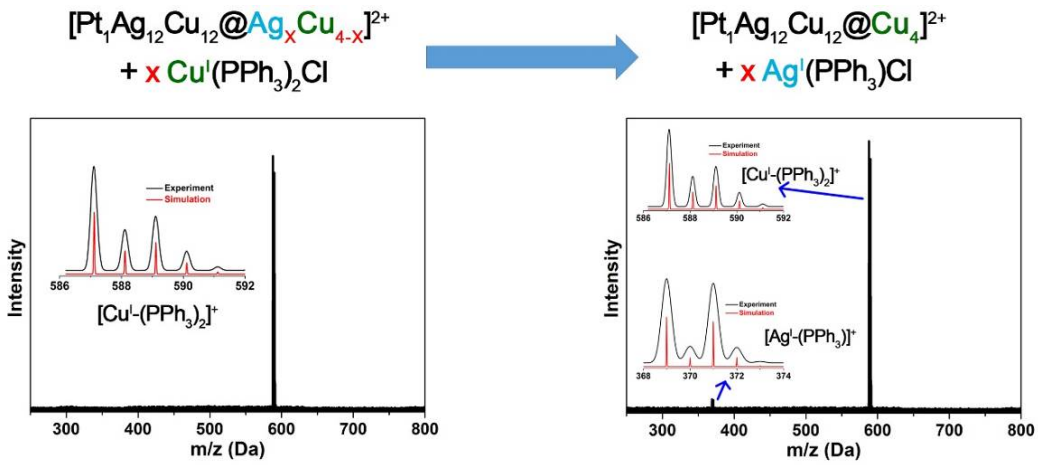

Fig. S8 ESI-MS spectra of $[Cu^{I}\text{-}(PPh_3)_2]^+$ and the metal-exchanged products (i.e., the mixture of $[Cu^{I}\text{-}(PPh_3)_2]^+$ and $[Ag^{I}\text{-}(PPh_3)]^+$. It should be noted that the $[Ag^{I}\text{-}(PPh_3)]^+$ is from the $Pt_1Ag_{12}Cu_{12}@Ag_xCu_{4-x}$ nanoclusters. The reaction equation is: $Pt_1Ag_{12}Cu_{12}@Ag_xCu_{4-x}$ + *x* $Cu^{I}(PPh_3)_2Cl$ → $Pt_1Ag_{12}Cu_{12}@Cu_4$ + *x* $Ag^{I}(PPh_3)Cl$.

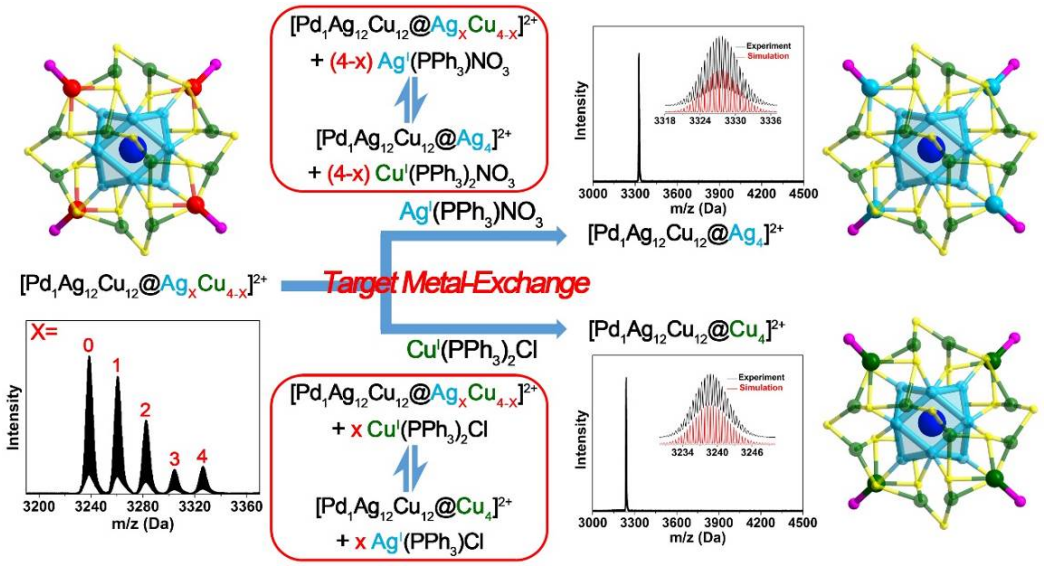

Fig. S9 Structures and ESI-MS spectra of $Pd_1Ag_{12}Cu_{12}@Ag_xCu_{4-x}$ (x = 0-4) and its metal-exchanged products: tri-metallic $Pd_1Ag_{16}Cu_{12}$ and $Pd_1Ag_{12}Cu_{16}$ nanoclusters with mono-dispersity. Insets: experimental and simulated isotope patterns of each nanocluster. Red boxes: schematic illustration of the metal-exchange process (also the size-concentration process). Color codes: cerulean sphere, Ag; blue sphere, Pd; green sphere, Cu; red sphere, mixed Ag/Cu; yellow sphere, S; purple sphere, P. For clarity, the carbon and hydrogen atoms are not shown.

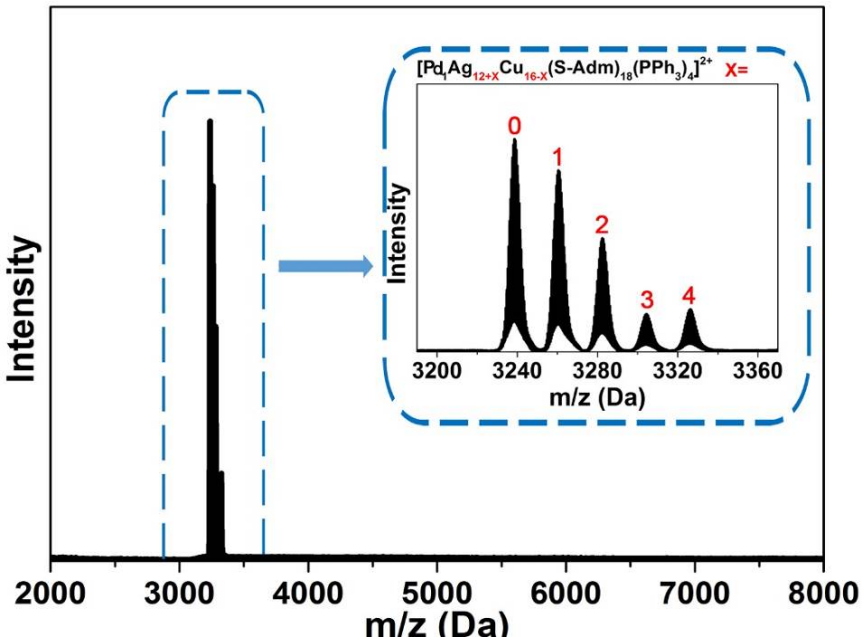

Fig. S10 Expansion of the ESI-MS spectrum in 2000-8000 Da (inset: 3190-3370 Da range) mass range of the $[Pd_1Ag_{12+x}Cu_{16-x}(S\text{-}Adm)_{18}(PPh_3)_4]^{2+}$ (x = 0-4) nanoclusters.

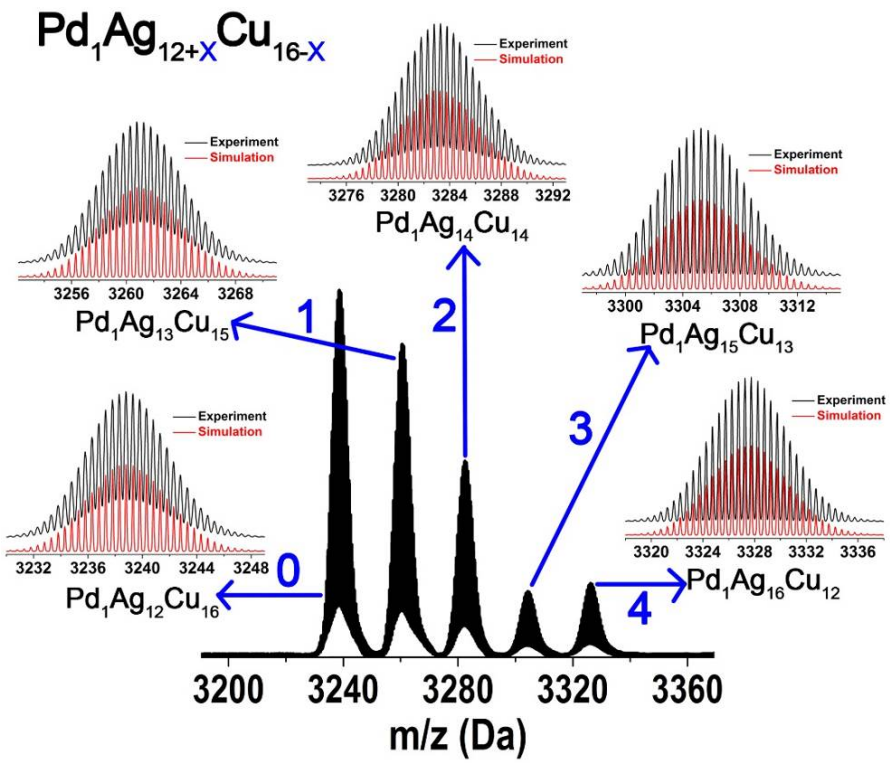

Fig. S11 ESI-MS spectrum in 3190-3370 Da mass range of the $[Pd_1Ag_{12+x}Cu_{16-x}(S\text{-}Adm)_{18}(PPh_3)_4]^{2+}$ (x = 0-4) nanoclusters. Insets: the experimental (black) and simulated (red) isotope patterns of each component in this mixture.

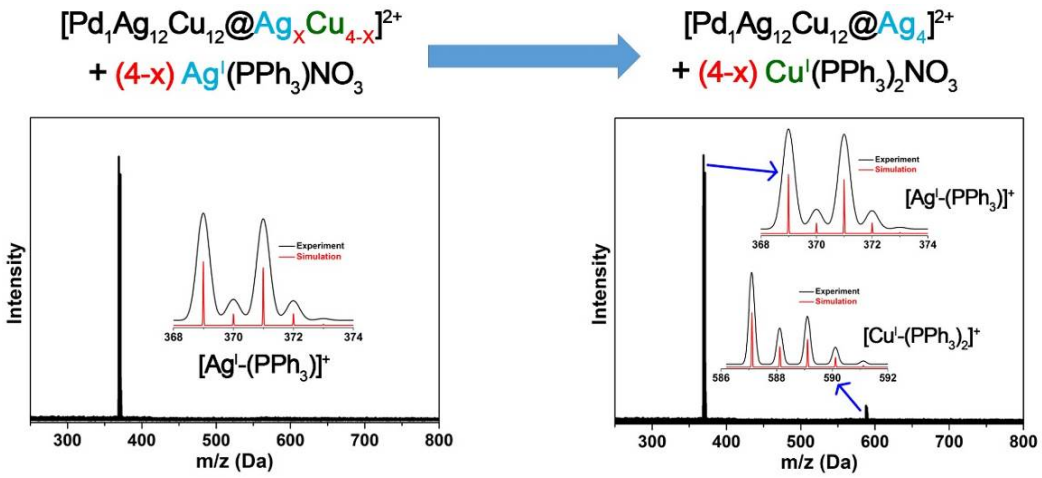

Fig. S12 ESI-MS spectra of $[Ag^{I}\text{-}(PPh_3)]^+$ and the metal-exchanged products (i.e., the mixture of $[Ag^{I}\text{-}(PPh_3)]^+$ and $[Cu^{I}\text{-}(PPh_3)_2]^+$. It should be noted that the $[Cu^{I}\text{-}(PPh_3)_2]^+$ is from the $Pd_1Ag_{12}Cu_{12}@Ag_xCu_{4-x}$ nanoclusters. The reaction equation is: $Pd_1Ag_{12}Cu_{12}@Ag_xCu_{4-x}$ + (4-x) $Ag^{I}(PPh_3)NO_3$ → $Pd_1Ag_{12}Cu_{12}@Ag_4$ + (4-x) $Cu^{I}(PPh_3)_2NO_3$.

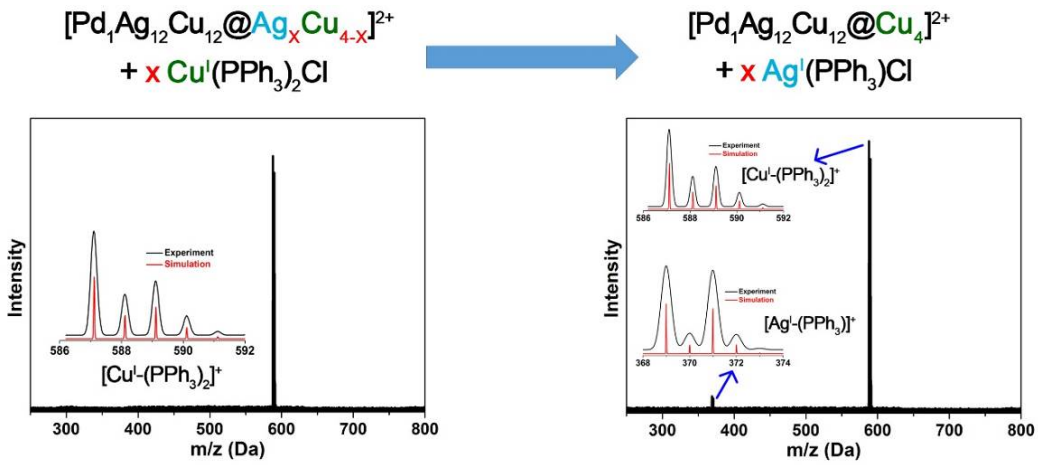

Fig. S13 ESI-MS spectra of $[Cu^{I}\text{-}(PPh_3)_2]^+$ and the metal-exchanged products (i.e., the mixture of $[Cu^{I}\text{-}(PPh_3)_2]^+$ and $[Ag^{I}\text{-}(PPh_3)]^+$. It should be noted that the $[Ag^{I}\text{-}(PPh_3)]^+$ is from the $Pd_1Ag_{12}Cu_{12}@Ag_xCu_{4-x}$ nanoclusters. The reaction equation is: $Pd_1Ag_{12}Cu_{12}@Ag_xCu_{4-x}$ + *x* $Cu^{I}(PPh_3)_2Cl \rightarrow Pd_1Ag_{12}Cu_{12}@Cu_4$ + *x* $Ag^{I}(PPh_3)Cl$.

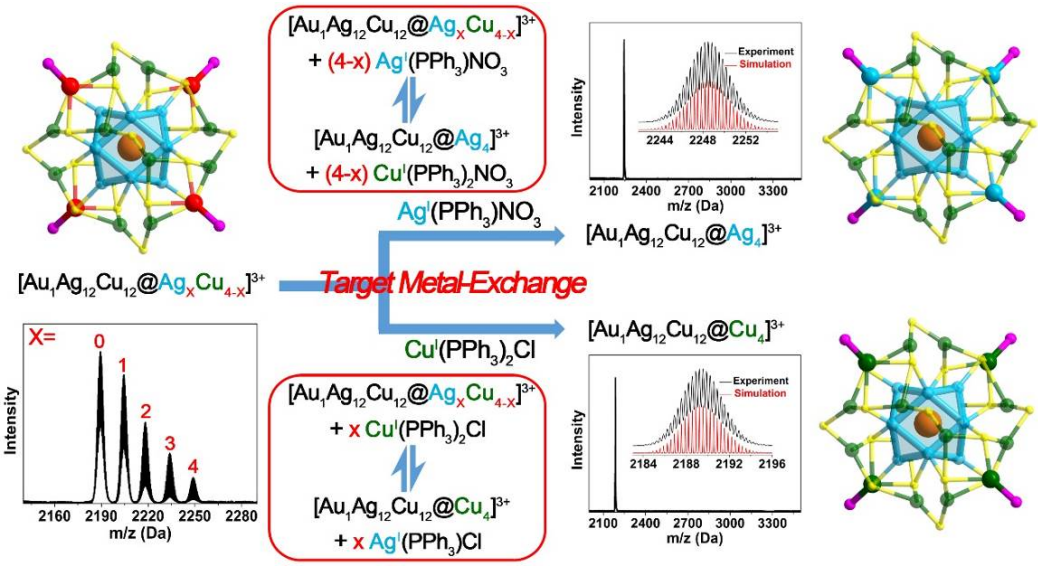

Fig. S14 Structures and ESI-MS spectra of $Au_1Ag_{12}Cu_{12}@Ag_xCu_{4-x}$ (*x* = 0-4) and its metal-exchanged products: tri-metallic $Au_1Ag_{16}Cu_{12}$ and $Au_1Ag_{12}Cu_{16}$ nanoclusters with mono-dispersity. Insets: experimental and simulated isotope patterns of each nanocluster. Red boxes: schematic illustration of the metal-exchange process (also the size-concentration process). Color codes: cerulean sphere, Ag; orange sphere, Au; green sphere, Cu; red sphere, mixed Ag/Cu; yellow sphere, S; purple sphere, P. For clarity, the carbon and hydrogen atoms are not shown.

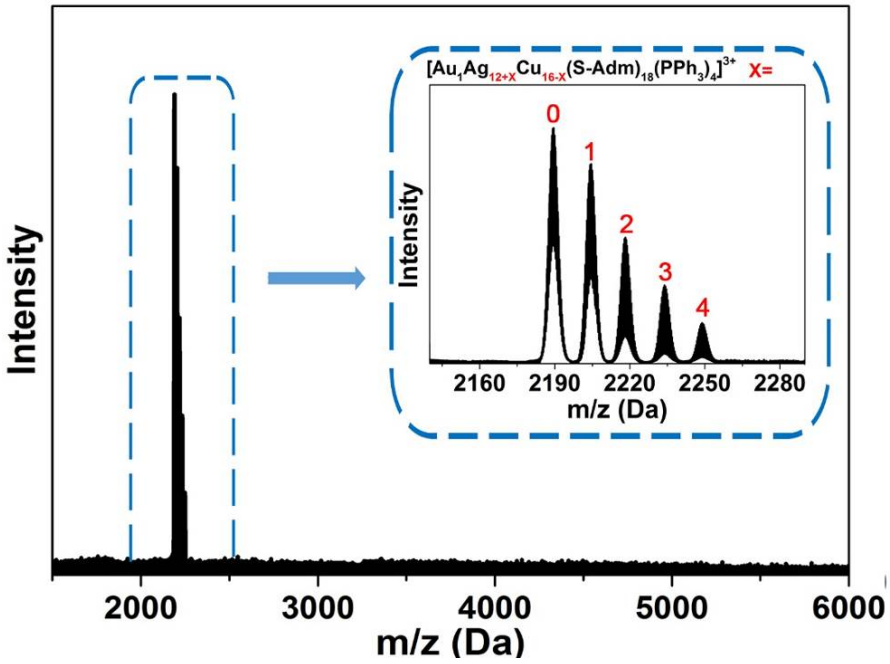

Fig. S15 Expansion of the ESI-MS spectrum in 1500-6000 Da (inset: 2140-2295 Da range) mass range of the $[Au_1Ag_{12+x}Cu_{16-x}(S\text{-}Adm)_{18}(PPh_3)_4]^{3+}$ (x = 0-4) nanoclusters.

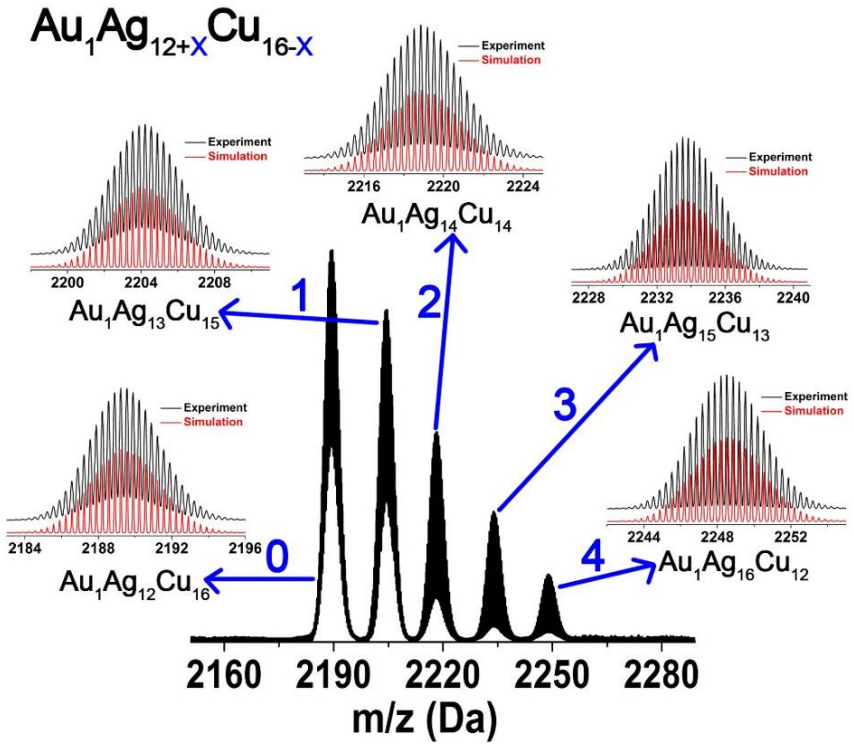

Fig. S16 ESI-MS spectrum in 3190-3370 Da mass range of the $[Au_1Ag_{12+x}Cu_{16-x}(S\text{-}Adm)_{18}(PPh_3)_4]^{2+}$ (x = 0-4) nanoclusters. Insets: the experimental (black) and simulated (red) isotope patterns of each component in this mixture.

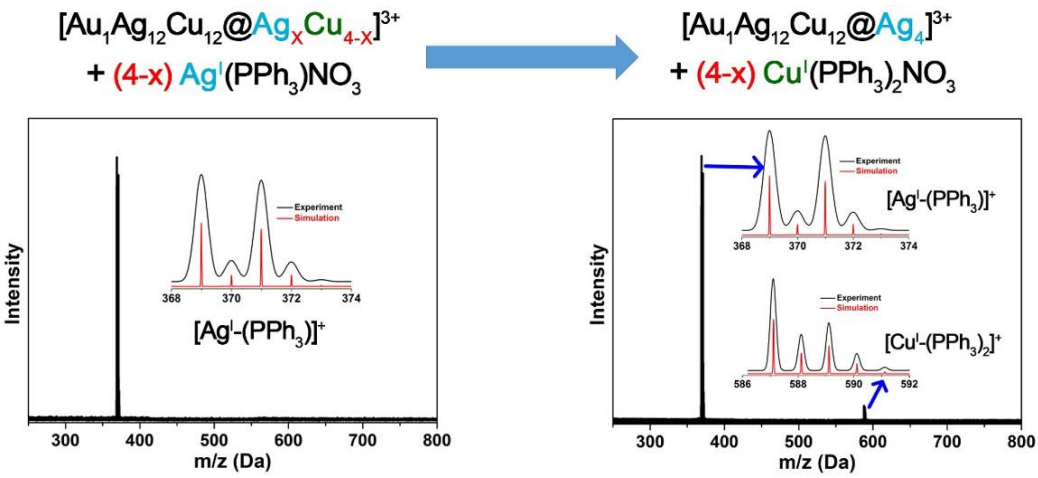

Fig. S17 ESI-MS spectra of $[Ag^{I}\text{-}(PPh_3)]^+$ and the metal-exchanged products (i.e., the mixture of $[Ag^{I}\text{-}(PPh_3)]^+$ and $[Cu^{I}\text{-}(PPh_3)_2]^+$. It should be noted that the $[Cu^{I}\text{-}(PPh_3)_2]^+$ is from the $Au_1Ag_{12}Cu_{12}@Ag_xCu_{4-x}$ nanoclusters. The reaction equation is: $Au_1Ag_{12}Cu_{12}@Ag_xCu_{4-x}$ + (4-*x*) $Ag^{I}(PPh_3)NO_3$ → $Au_1Ag_{12}Cu_{12}@Ag_4$ + (4-*x*) $Cu^{I}(PPh_3)_2NO_3$.

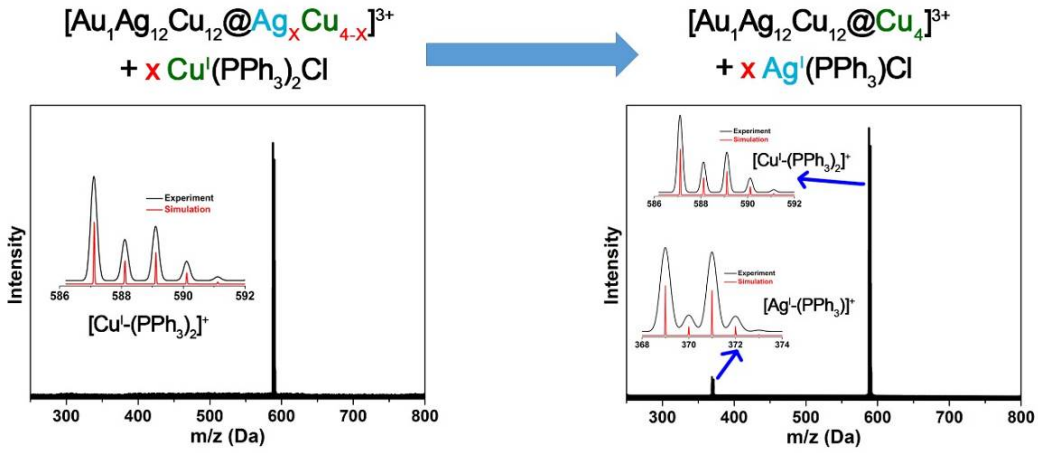

Fig. S18 ESI-MS spectra of $[Cu^{I}\text{-}(PPh_3)_2]^+$ and the metal-exchanged products (i.e., the mixture of $[Cu^{I}\text{-}(PPh_3)_2]^+$ and $[Ag^{I}\text{-}(PPh_3)]^+$. It should be noted that the $[Ag^{I}\text{-}(PPh_3)]^+$ is from the $Au_1Ag_{12}Cu_{12}@Ag_xCu_{4-x}$ nanoclusters. The reaction equation is: $Au_1Ag_{12}Cu_{12}@Ag_xCu_{4-x}$ + *x* $Cu^{I}(PPh_3)_2Cl$ → $Au_1Ag_{12}Cu_{12}@Cu_4$ + *x* $Ag^{I}(PPh_3)Cl$.

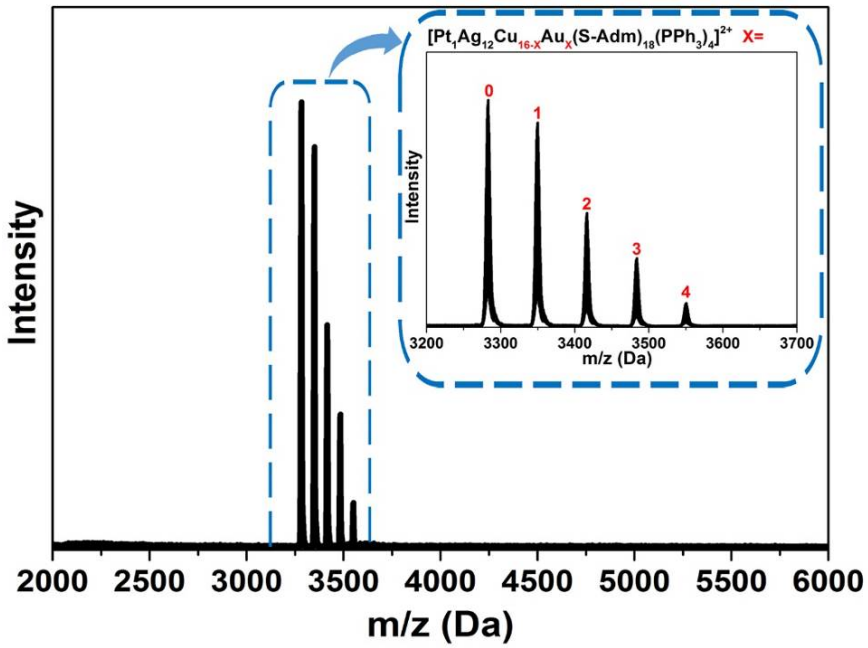

Fig. S19 Expansion of the ESI-MS spectrum in 2000-6000 Da (inset: 3200-3700 Da range) mass range of the $[Pt_1Ag_{12}Cu_{16-x}Au_x(S\text{-}Adm)_{18}(PPh_3)_4]^{3+}$ (x = 0-4) nanoclusters.

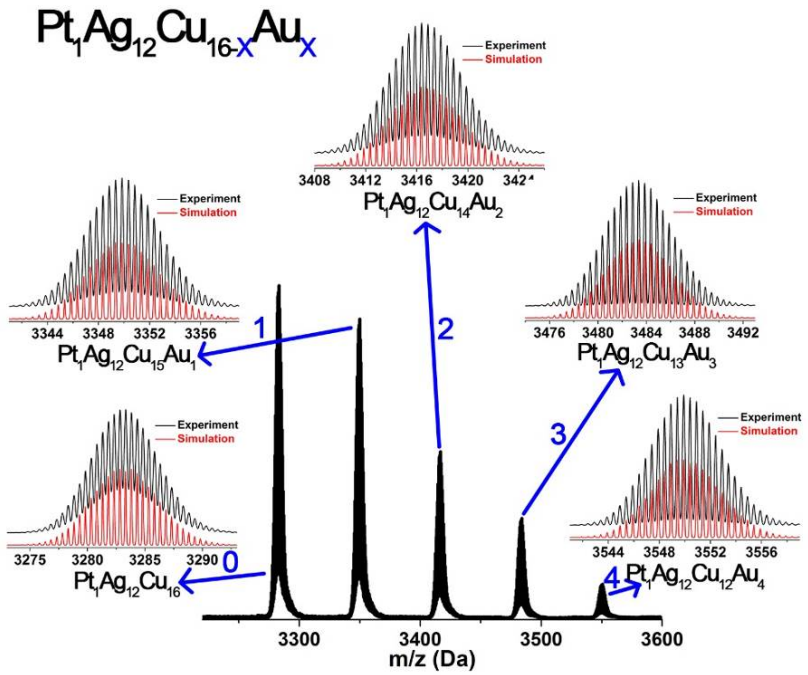

Fig. S20 ESI-MS spectrum in 3200-3700 Da mass range of the $[Pt_1Ag_{12}Cu_{16-x}Au_x(S\text{-}Adm)_{18}(PPh_3)_4]^{3+}$ (x = 0-4). Insets: the experimental (black) and simulated (red) isotope patterns of each component in this mixture.

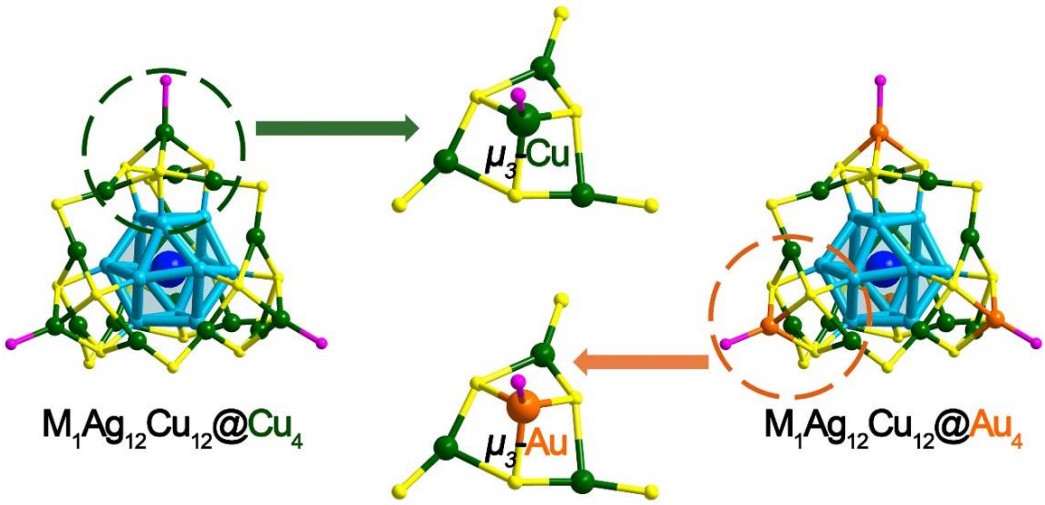

Fig. S21 Structures of μ_3-Cu and μ_3-Au in the vertical sites (i.e., $M_1(PPh_3)_1@Cu_3(S\text{-}Adm)_6$, M= Cu/Au). Color codes: cerulean sphere, Ag; blue sphere, Pd; green sphere, Cu; orange sphere, Au; yellow sphere, S; purple sphere, P. For clarity, the carbon and hydrogen atoms are not shown.

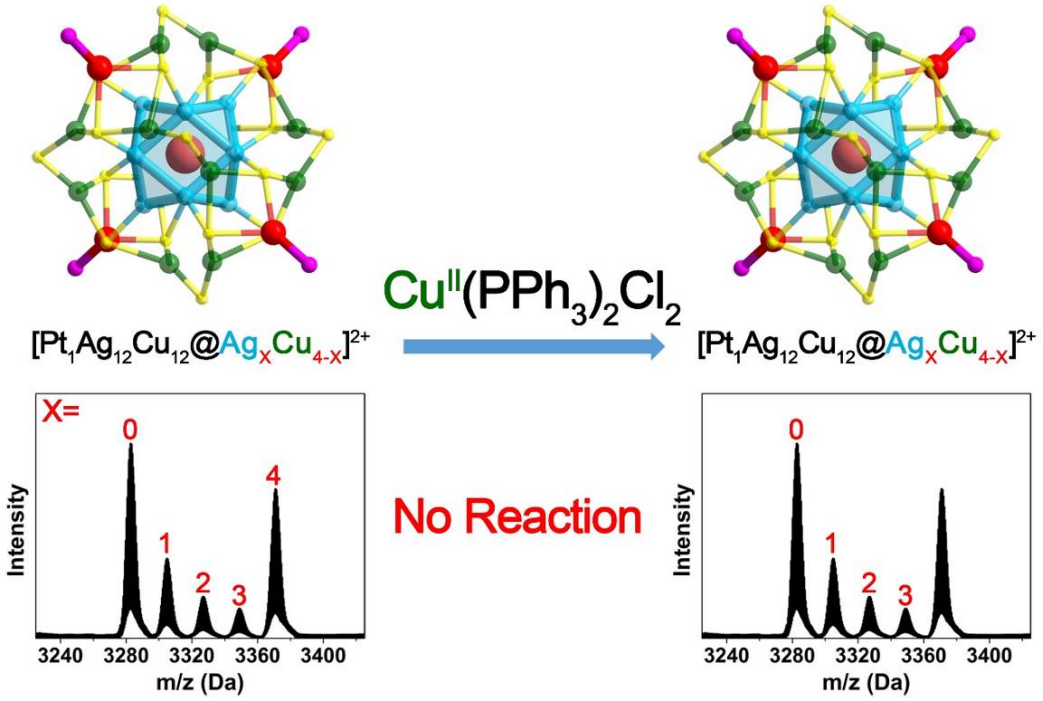

Fig. S22 Schematic illustration of the no coordination ability of the Cu(II) in the vertical sites, and thus the composition of $Pt_1Ag_{12}Cu_{12}@Ag_xCu_{4-x}$ nanoclusters maintains. Color codes: cerulean sphere, Ag; pink sphere, Pt; green sphere, Cu; red sphere, mixed Ag/Cu; yellow sphere, S; purple sphere, P. For clarity, the carbon and hydrogen atoms are not shown.

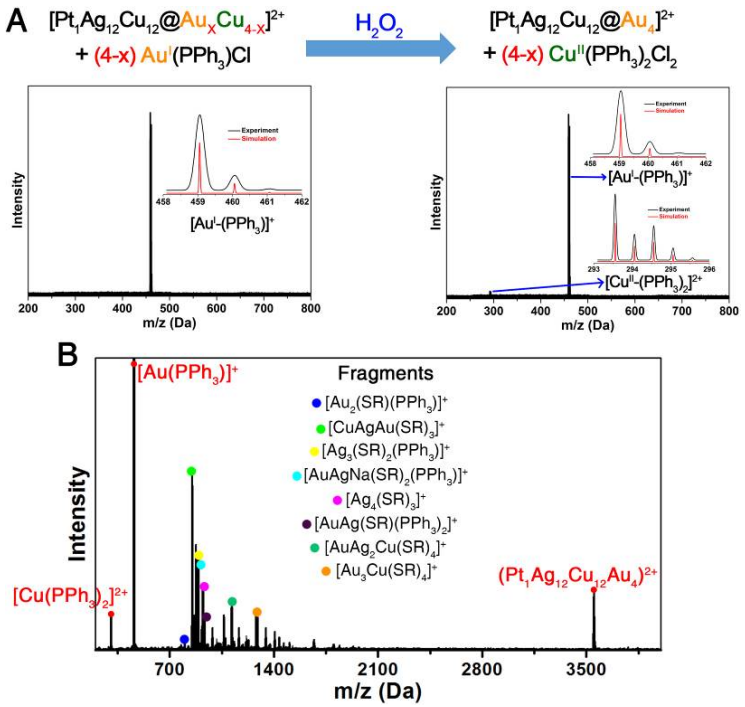

Fig. S23 (A) ESI-MS spectra of $[Au^{I}\text{-}(PPh_3)]^+$ and the metal-exchanged products (i.e., the mixture of $[Cu^{II}\text{-}(PPh_3)_2]^+$ and $[Au^{I}\text{-}(PPh_3)]^+$. It should be noted that the $[Cu^{II}\text{-}(PPh_3)_2]^+$ is from the $Au_1Ag_{12}Cu_{12}@Au_xCu_{4-x}$ nanoclusters. (B) Fragments of decomposed nanoclusters in reacting the $Pt_1Ag_{12}Cu_{12}(SR)_{18}Cu_4(PPh_3)_4$ nanocluster with $Au^{I}(PPh_3)Cl$ and H_2O_2 (without purification).

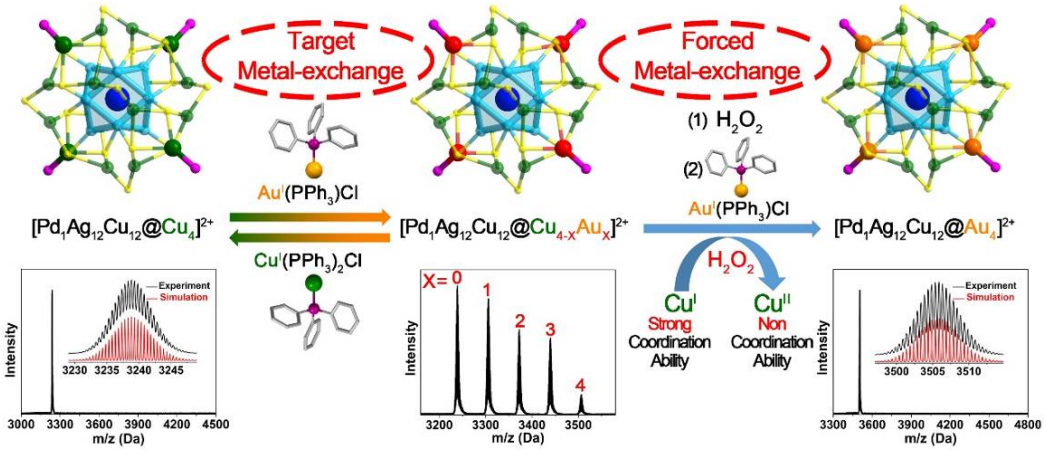

Fig. S24 Illustration of the synthetic procedures from $Pd_1Ag_{12}Cu_{16}$ to poly-dispersed $Pd_1Ag_{12}Cu_{16-x}Au_x$ (x = 0-4), and then to mono-dispersed $Pd_1Ag_{12}Cu_{12}Au_4$ nanocluster. The blue curve represents the oxidation from Cu(I) to Cu(II) induced by H_2O_2, thus the non-coordinate ability of Cu(II) leads to the mono-dispersity of the final tetra-metallic $Pd_1Ag_{12}Cu_{12}Au_4$ nanocluster. Color codes: cerulean sphere, Ag; blue sphere, Pd; orange sphere, Au; green sphere, Cu; red sphere, mixed Au/Cu; yellow sphere, S; purple sphere, P. For clarity, the carbon and hydrogen atoms are not shown.

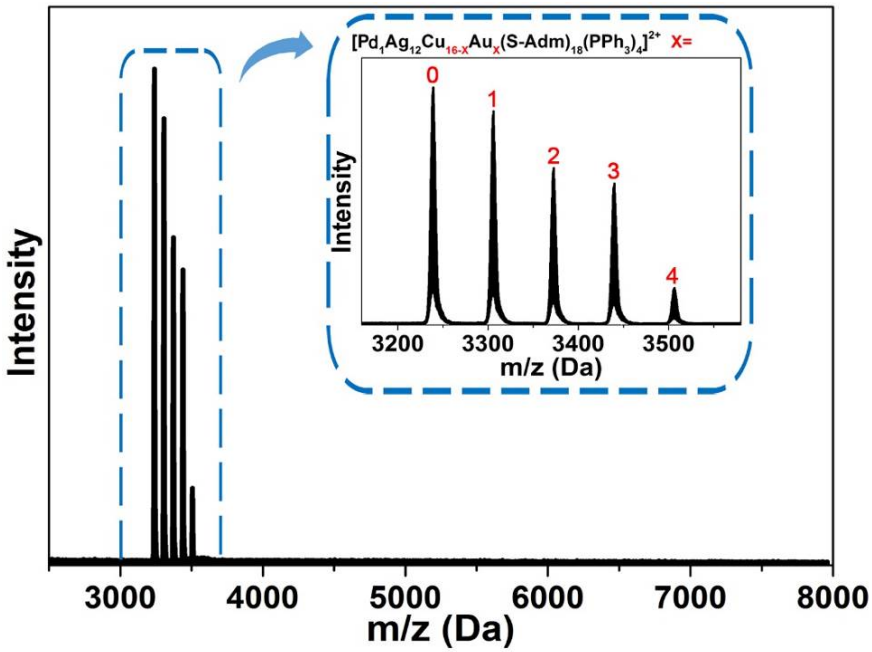

Fig. S25 Expansion of the ESI-MS spectrum in 2500-8000 Da (inset: 3150-3650 Da range) mass range of the $[Pd_1Ag_{12}Cu_{16-x}Au_x(S\text{-}Adm)_{18}(PPh_3)_4]^{3+}$ (x = 0-4) nanoclusters.

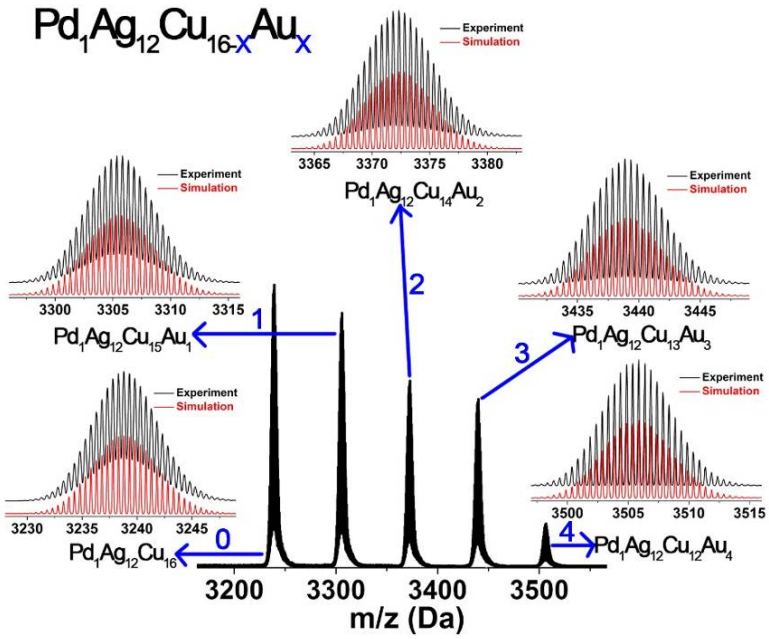

Fig. S26 ESI-MS spectrum in 3150-3650 Da mass range of the $[Pd_1Ag_{12}Cu_{16-x}Au_x(S\text{-}Adm)_{18}(PPh_3)_4]^{3+}$ (x = 0-4). Insets: the experimental (black) and simulated (red) isotope patterns of each component in this mixture.

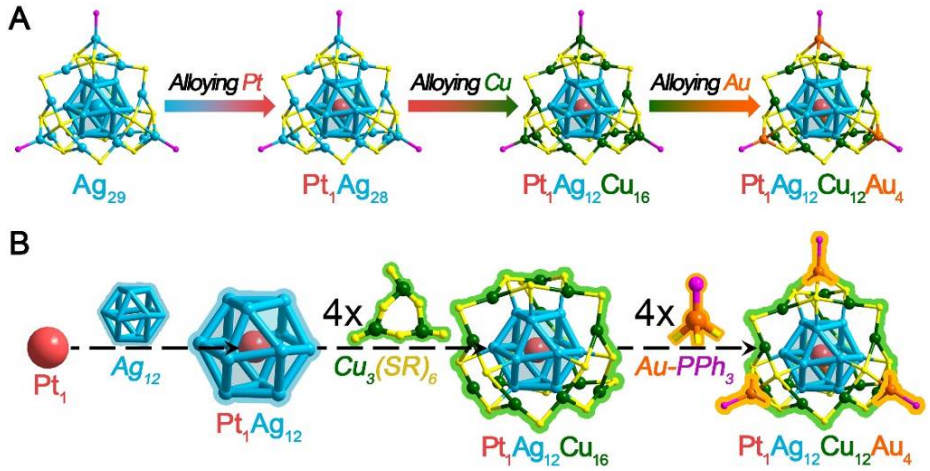

Fig. S27 (A) Illustration of the systematic M_{29} nanosystem. Note that there are a total of three nanosystems, i.e., Pt-centered, Pd-centered, and Au-centered M_{29} nanosystems. Here we only show part of the Pt-centered nanosystem, including the mono-metallic Ag_{29}, bi-metallic Pt_1Ag_{28}, tri-metallic $Pt_1Ag_{12}Cu_{16}$, and tetra-metallic $Pt_1Ag_{12}Cu_{12}Au_4$ nanoclusters. (B) Structural anatomy of the tetra-metallic $Pt_1Ag_{12}Cu_{12}Au_4$ nanocluster with the Pt (center)@Ag_{12}(1^{st}-shell)@Cu_{12}(2^{nd}-shell)@Au_4(vertex) tetra-stratified arrangement. Color codes: cerulean sphere, Ag; pink sphere, Pt; orange sphere, Au; green sphere, Cu; yellow sphere, S; purple sphere, P. For clarity, the carbon and hydrogen atoms are not shown.

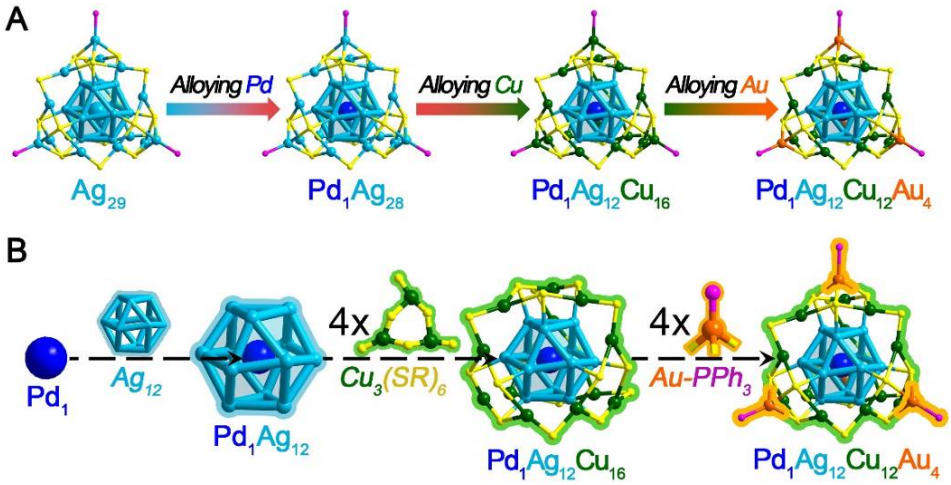

Fig. S28 (A) Illustration of the M_{29} nanosystem. Noted that there are a total of three nanosystems, i.e., Pt-centered, Pd-centered, and Au-centered M_{29} nanosystems. There we just show part of the Pd-centered nanosyntem, including the mono-metallic Ag_{29}, bi-metallic Pd_1Ag_{28}, tri-metallic $Pd_1Ag_{12}Cu_{16}$, and tetra-metallic $Pd_1Ag_{12}Cu_{12}Au_4$ nanoclusters. (B) Structural anatomy of the tetra-metallic $Pd_1Ag_{12}Cu_{12}Au_4$ nanocluster with the Pd (center)@Ag_{12}(1^{st}-shell)@Cu_{12}(2^{nd}-shell)@Au_4(vertex) tetra-stratified arrangement. Color codes: cerulean sphere, Ag; blue sphere, Pd; orange sphere, Au; green sphere, Cu; yellow sphere, S; purple sphere, P. For clarity, the carbon and hydrogen atoms are not shown.

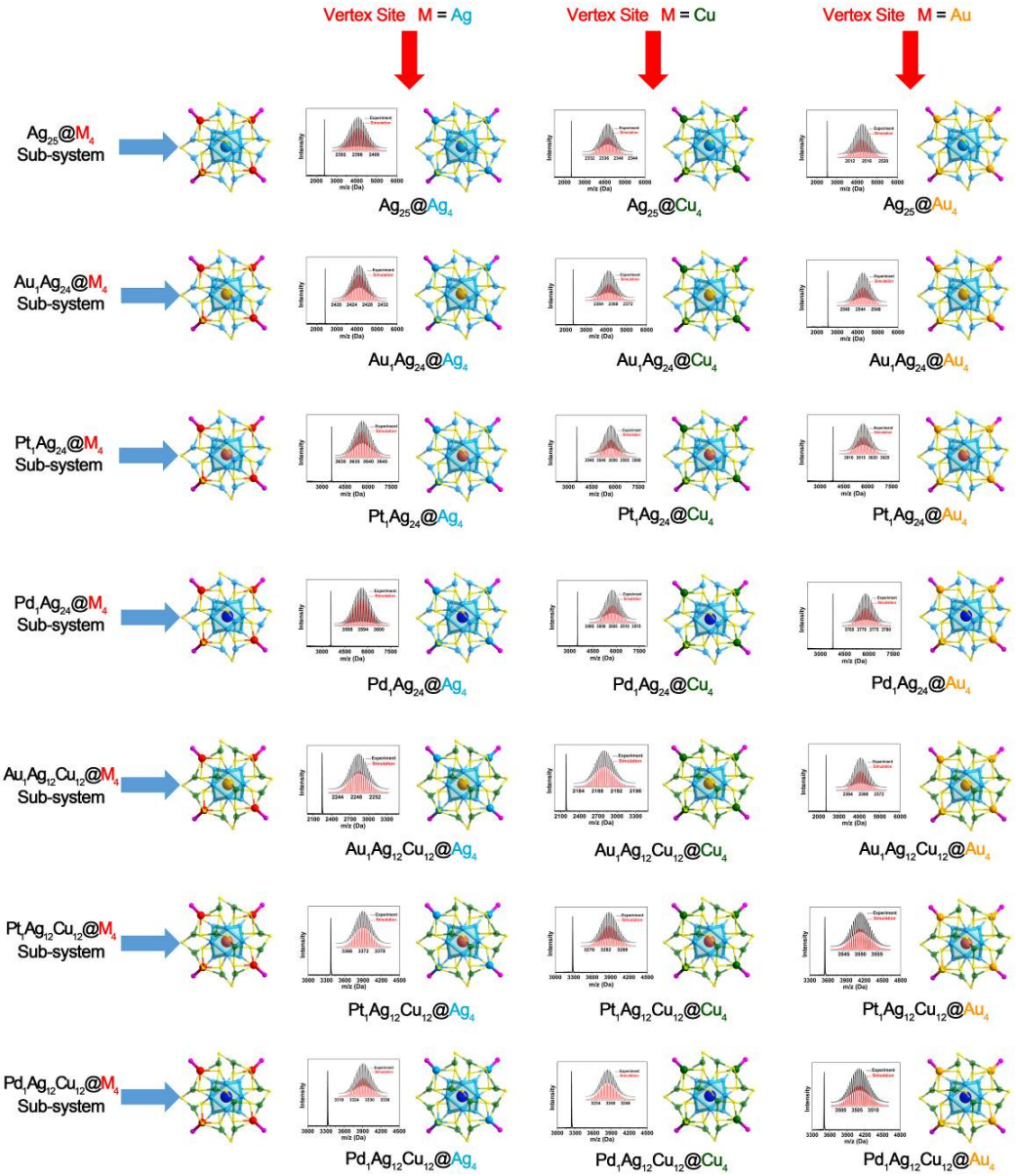

Fig. S29 Overview of the M_{29} (M = Ag/Cu/Pt/Pd/Au) nanocluster library. Comparison of the ESI-MS spectra and structural configurations of these M_{29} nanoclusters. These nanoclusters could be classified into 7 sub-systems by classifying the metal arrangement. Blue arrows represent the nanoclusters with the same center@1st-shell@2nd-shell arrangements but with different vertex atoms (Ag/Cu/Au). Each sub-system contains three nanoclusters (*i.e.*, with Ag, Cu or Au vertex occupation (red arrows)). Color codes: cerulean sphere, Ag; green sphere, Cu; pink sphere, Pt; blue sphere, Pd; orange sphere, Au; yellow sphere, S; purple sphere, P. For clarity, the C and H atoms are omitted.

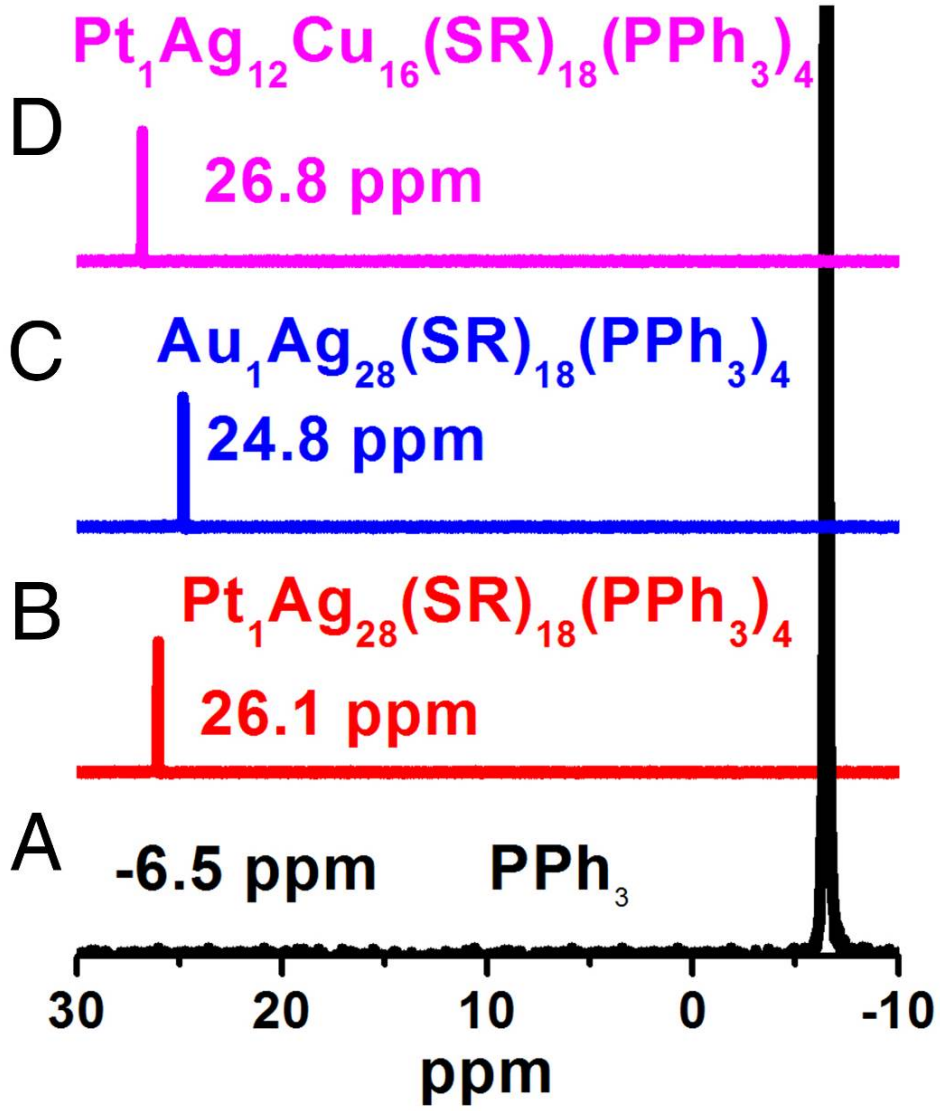

Fig. S30 ^{31}P NMR spectra of (A) PPh_3 ligand, (B) $Pt_1Ag_{28}(SR)_{18}(PPh_3)_4$ nanocluster, (C) $Au_1Ag_{28}(SR)_{18}(PPh_3)_4$ nanocluster, and (D) $Pt_1Ag_{12}Cu_{16}(SR)_{18}(PPh_3)_4$ nanocluster. Samples are dissolved in CD_2Cl_2.

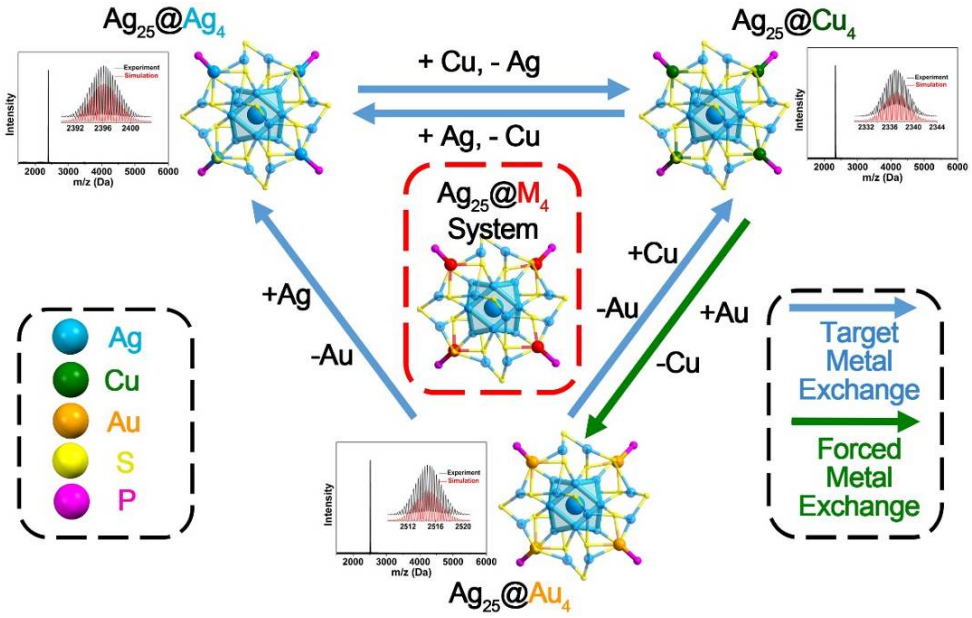

Fig. S31 Illustration (with structures and ESI-MS spectra) of the $Ag_{25}@M_4$ nanosystem composed by Ag_{29}, $Ag_{25}Cu_4$ and $Ag_{25}Au_4$ nanoclusters. Insets of the ESI-MS data: experimental and simulated isotope patterns of each nanocluster. The blue and green arrows indicate the alloying modes with target metal exchange and forced metal exchange. Color codes: cerulean sphere, Ag; orange sphere, Au; green sphere, Cu; yellow sphere, S; purple sphere, P. For clarity, the carbon and hydrogen atoms are not shown.

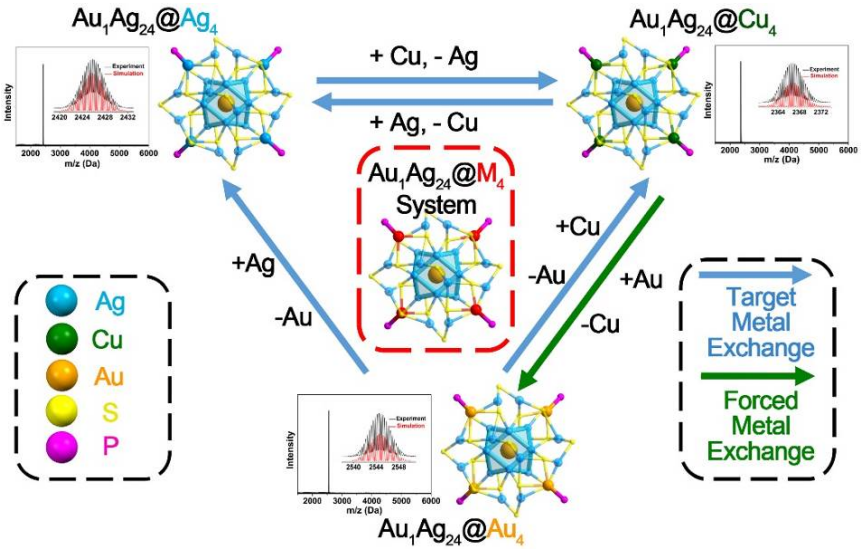

Fig. S32 Illustration (with structures and ESI-MS spectra) of the $Au_1Ag_{24}@M_4$ nanosystem composed by Au_1Ag_{28}, $Au_1Ag_{24}Cu_4$ and Au_5Ag_{24} nanoclusters. Insets of the ESI-MS data: experimental and simulated isotope patterns of each nanocluster. The blue and green arrows indicate the alloying modes with target metal exchange and forced metal exchange. Color codes: cerulean sphere, Ag; orange sphere, Au; green sphere, Cu; yellow sphere, S; purple sphere, P. For clarity, the carbon and hydrogen atoms are not shown.

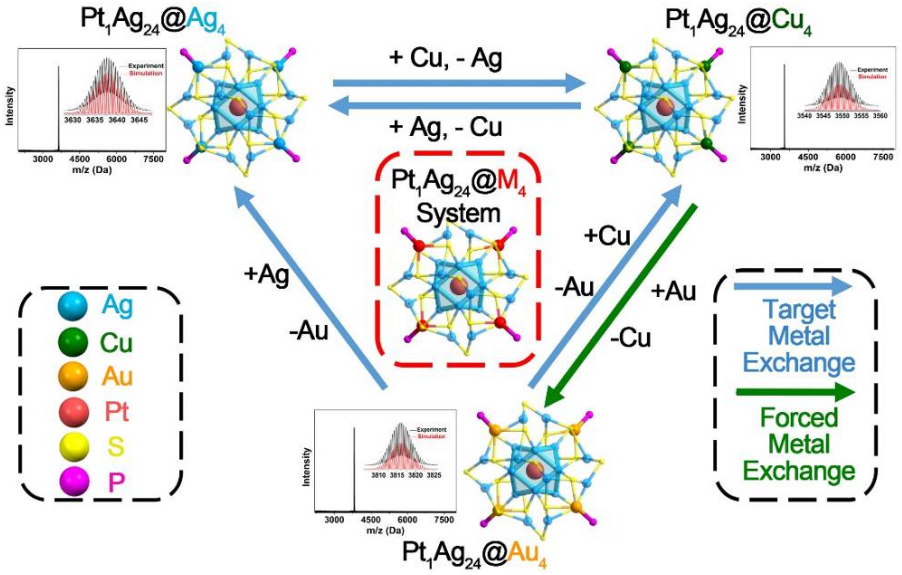

Fig. S33 Illustration (with structures and ESI-MS spectra) of the $Pt_1Ag_{24}@M_4$ nanosystem composed by Pt_1Ag_{28}, $Pt_1Ag_{24}Cu_4$ and $Pt_1Ag_{24}Au_4$ nanoclusters. Insets of the ESI-MS data: experimental and simulated isotope patterns of each nanocluster. The blue and green arrows indicate the alloying modes with target metal exchange and forced metal exchange. Color codes: pink sphere, Pt; cerulean sphere, Ag; orange sphere, Au; green sphere, Cu; yellow sphere, S; purple sphere, P. For clarity, the carbon and hydrogen atoms are not shown.

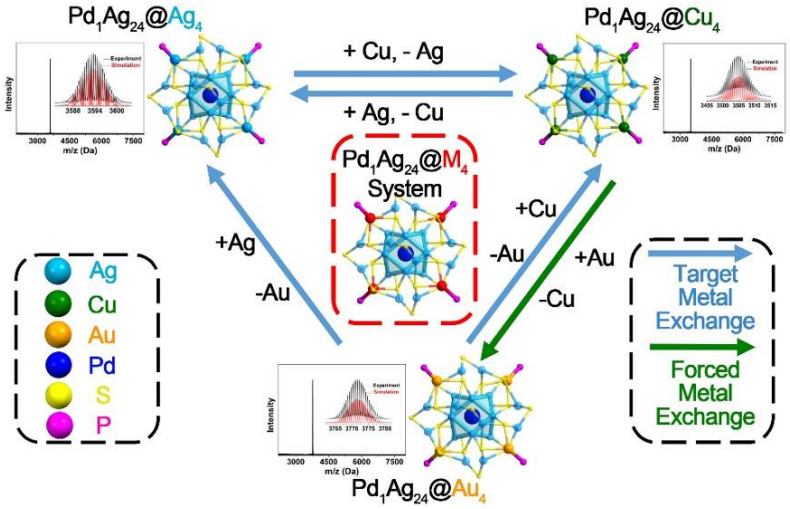

Fig. S34 Illustration (with structures and ESI-MS spectra) of the $Pd_1Ag_{24}@M_4$ nanosystem composed by Pd_1Ag_{28}, $Pd_1Ag_{24}Cu_4$ and $Pd_1Ag_{24}Au_4$ nanoclusters. Insets of the ESI-MS data: experimental and simulated isotope patterns of each nanocluster. The blue and green arrows indicate the alloying modes with target metal exchange and forced metal exchange. Color codes: cerulean sphere, Ag; blue sphere, Pd; orange sphere, Au; green sphere, Cu; yellow sphere, S; purple sphere, P. For clarity, the carbon and hydrogen atoms are not shown.

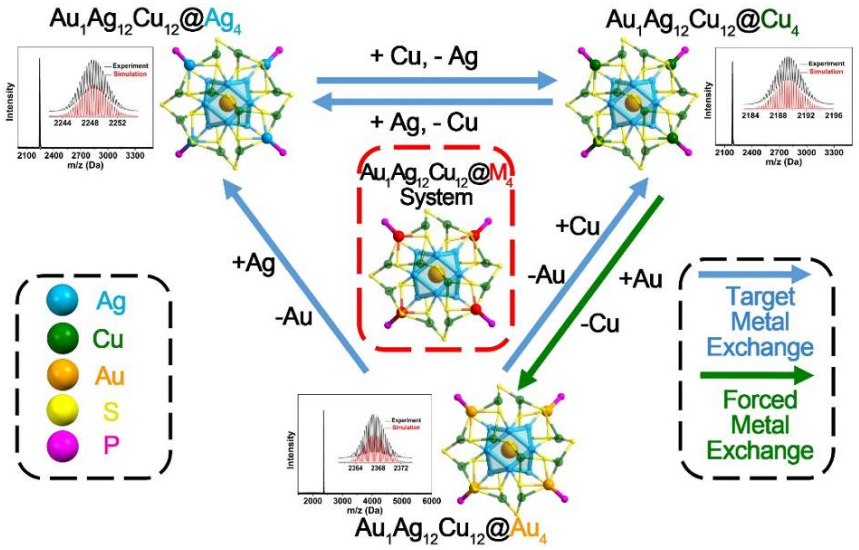

Fig. S35 Illustration (with structures and ESI-MS spectra) of the $Au_1Ag_{12}Cu_{12}@M_4$ nanosystem composed by $Au_1Ag_{16}Cu_{12}$, $Au_1Ag_{12}Cu_{16}$ and $Au_5Ag_{12}Cu_{12}$ nanoclusters. Insets of the ESI-MS data: experimental and simulated isotope patterns of each nanocluster. The blue and green arrows indicate the alloying modes with target metal exchange and forced metal exchange. Color codes: cerulean sphere, Ag; orange sphere, Au; green sphere, Cu; yellow sphere, S; purple sphere, P. For clarity, the carbon and hydrogen atoms are not shown.

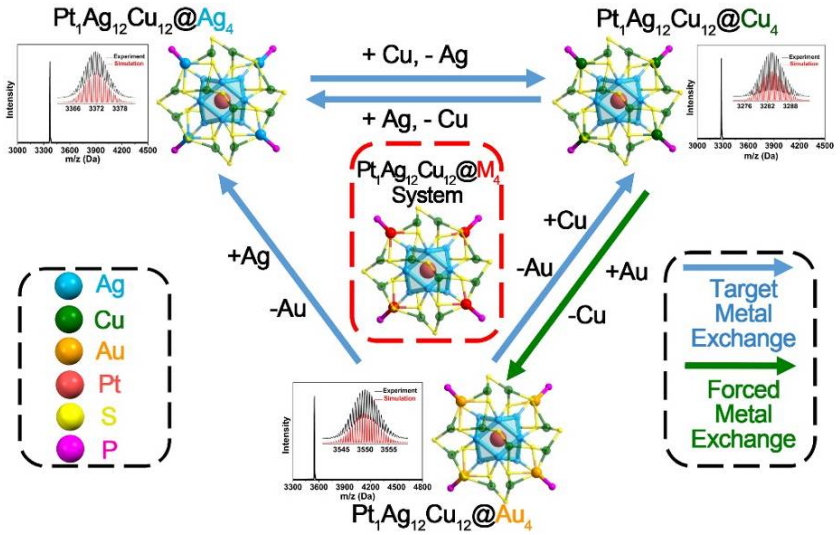

Fig. S36 Illustration (with structures and ESI-MS spectra) of the $Pt_1Ag_{12}Cu_{12}@M_4$ nanosystem composed by $Pt_1Ag_{16}Cu_{12}$, $Pt_1Ag_{12}Cu_{16}$ and $Pt_1Ag_{12}Cu_{12}Au_4$ nanoclusters. Insets of the ESI-MS data: experimental and simulated isotope patterns of each nanocluster. The blue and green arrows indicate the alloying modes with target metal exchange and forced metal exchange. Color codes: pink sphere, Pt; cerulean sphere, Ag; orange sphere, Au; green sphere, Cu; yellow sphere, S; purple sphere, P. For clarity, the carbon and hydrogen atoms are not shown.

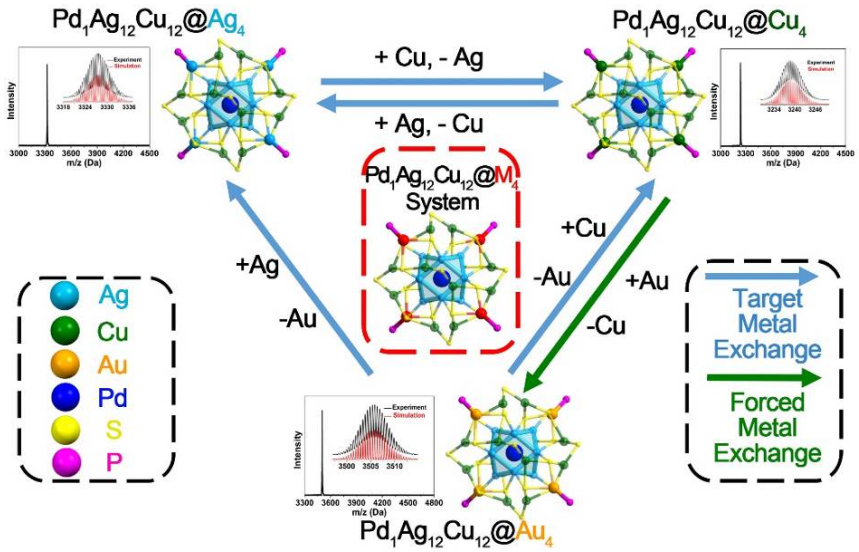

Fig. S37 Illustration (with structures and ESI-MS spectra) of the $Pd_1Ag_{12}Cu_{12}@M_4$ nanosystem composed by $Pd_1Ag_{16}Cu_{12}$, $Pd_1Ag_{12}Cu_{16}$ and $Pd_1Ag_{12}Cu_{12}Au_4$ nanoclusters. Insets of the ESI-MS data: experimental and simulated isotope patterns of each nanocluster. The blue and green arrows indicate the alloying modes with target metal exchange and forced metal exchange. Color legend: blue sphere, Pd; cerulean sphere, Ag; orange sphere, Au; green sphere, Cu; yellow sphere, S; purple sphere, P. For clarity, the carbon and hydrogen atoms are not shown.

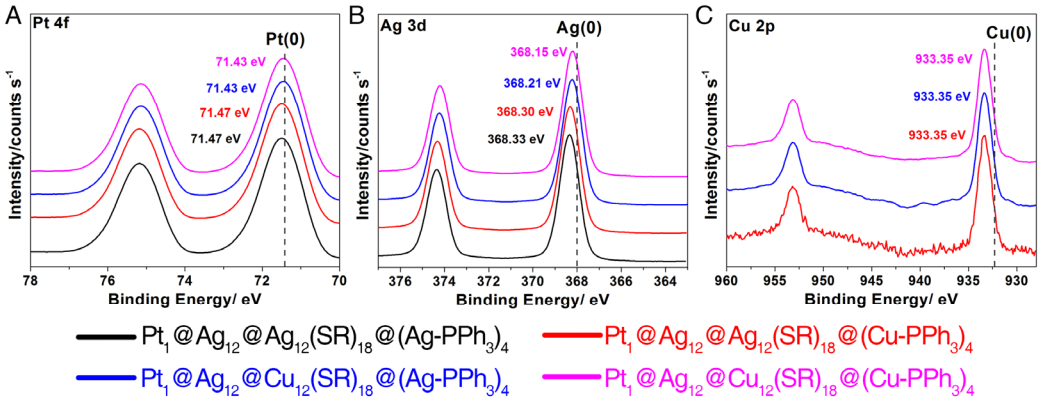

Fig. S38 XPS of Pt 4f, Ag 3d, and Cu 2p peaks in Pt-centered nanoclusters. Black lines: $Pt_1@Ag_{12}@Ag_{12}(SR)_{18}@(Ag\text{-}PPh_3)_4$ nanocluster; red lines: $Pt_1@Ag_{12}@Ag_{12}(SR)_{18}@(Cu\text{-}PPh_3)_4$ nanocluster; blue lines: $Pt_1@Ag_{12}@Cu_{12}(SR)_{18}@(Ag\text{-}PPh_3)_4$ nanocluster; purple lines: $Pt_1@Ag_{12}@Cu_{12}(SR)_{18}@(Cu\text{-}PPh_3)_4$ nanocluster.

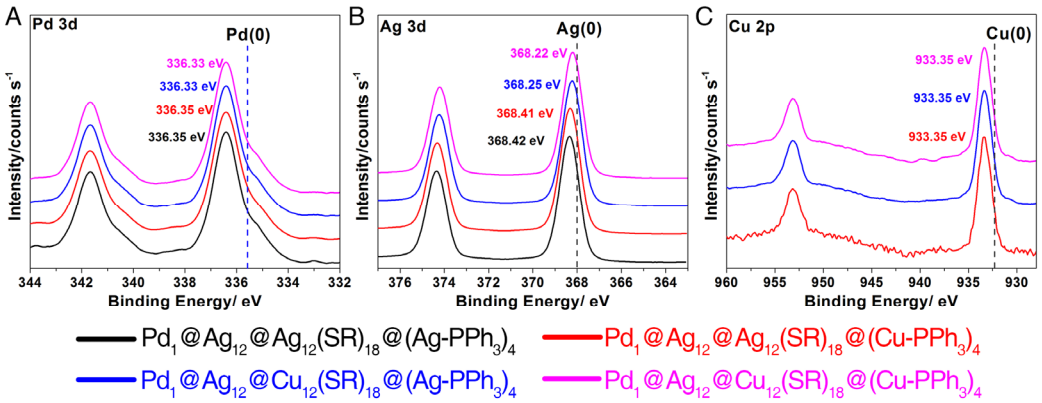

Fig. S39 XPS of Pd 3d, Ag 3d, and Cu 2p peaks in Pd-centered nanoclusters. Black lines: $Pd_1@Ag_{12}@Ag_{12}(SR)_{18}@(Ag\text{-}PPh_3)_4$ nanocluster; red lines: $Pd_1@Ag_{12}@Ag_{12}(SR)_{18}@(Cu\text{-}PPh_3)_4$ nanocluster; blue lines: $Pd_1@Ag_{12}@Cu_{12}(SR)_{18}@(Ag\text{-}PPh_3)_4$ nanocluster; purple lines: $Pd_1@Ag_{12}@Cu_{12}(SR)_{18}@(Cu\text{-}PPh_3)_4$ nanocluster.

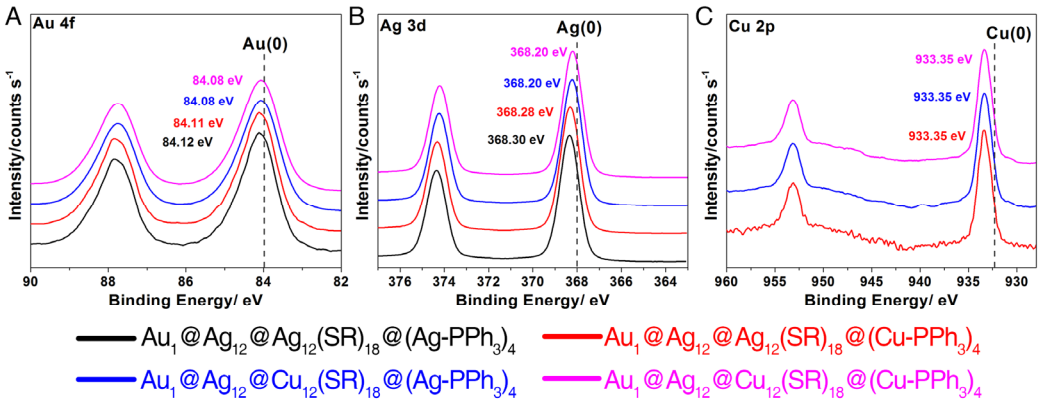

Fig. S40 XPS of Au 4f, Ag 3d, and Cu 2p peaks in Au-centered nanoclusters. Black lines: $Au_1@Ag_{12}@Ag_{12}(SR)_{18}@(Ag\text{-}PPh_3)_4$ nanocluster; red lines: $Au_1@Ag_{12}@Ag_{12}(SR)_{18}@(Cu\text{-}PPh_3)_4$ nanocluster; blue lines: $Au_1@Ag_{12}@Cu_{12}(SR)_{18}@(Ag\text{-}PPh_3)_4$ nanocluster; purple lines: $Au_1@Ag_{12}@Cu_{12}(SR)_{18}@(Cu\text{-}PPh_3)_4$ nanocluster. From the XPS results (Figs. S38-S40), we concluded that: (i) for the kernel atom (Pt/Pd/Au): altering the vertex metals between Ag and Cu has almost no effect on the XPS results of the kernel atom (*e.g.*, from $Pt_1@Ag_{12}@Ag_{12}(SR)_{18}@(Ag\text{-}PPh_3)_4$ to $Pt_1@Ag_{12}@Ag_{12}(SR)_{18}@(Cu\text{-}PPh_3)_4$); by comparison, the XPS peaks of the kernel atom blue-shift (shift to the M(0) peak) by altering the metals in 3rd-shell from Ag to Cu (*e.g.*, from $Pt_1@Ag_{12}@Ag_{12}(SR)_{18}@(Ag\text{-}PPh_3)_4$ to $Pt_1@Ag_{12}@Cu_{12}(SR)_{18}@(Ag\text{-}PPh_3)_4$). (ii) for the Ag atom: altering the vertex metals from Ag to Cu slightly blue-shift the XPS peak of Ag (*e.g.*, from $Pt_1@Ag_{12}@Ag_{12}(SR)_{18}@(Ag\text{-}PPh_3)_4$ to $Pt_1@Ag_{12}@Ag_{12}(SR)_{18}@(Cu\text{-}PPh_3)_4$); by comparison, the Ag peak shows a significant blue-shift when the Ag atoms in the 3rd-shell are substituted by the Cu atoms (*e.g.*, from $Pt_1@Ag_{12}@Ag_{12}(SR)_{18}@(Ag\text{-}PPh_3)_4$ to $Pt_1@Ag_{12}@Cu_{12}(SR)_{18}@(Ag\text{-}PPh_3)_4$). (iii) for the Cu atom: the introduced Cu atoms can be only arranged at the 3rd shell or the vertex, and the XPS results demonstrated that all introduced Cu atoms display an almost unchanged oxidation state.

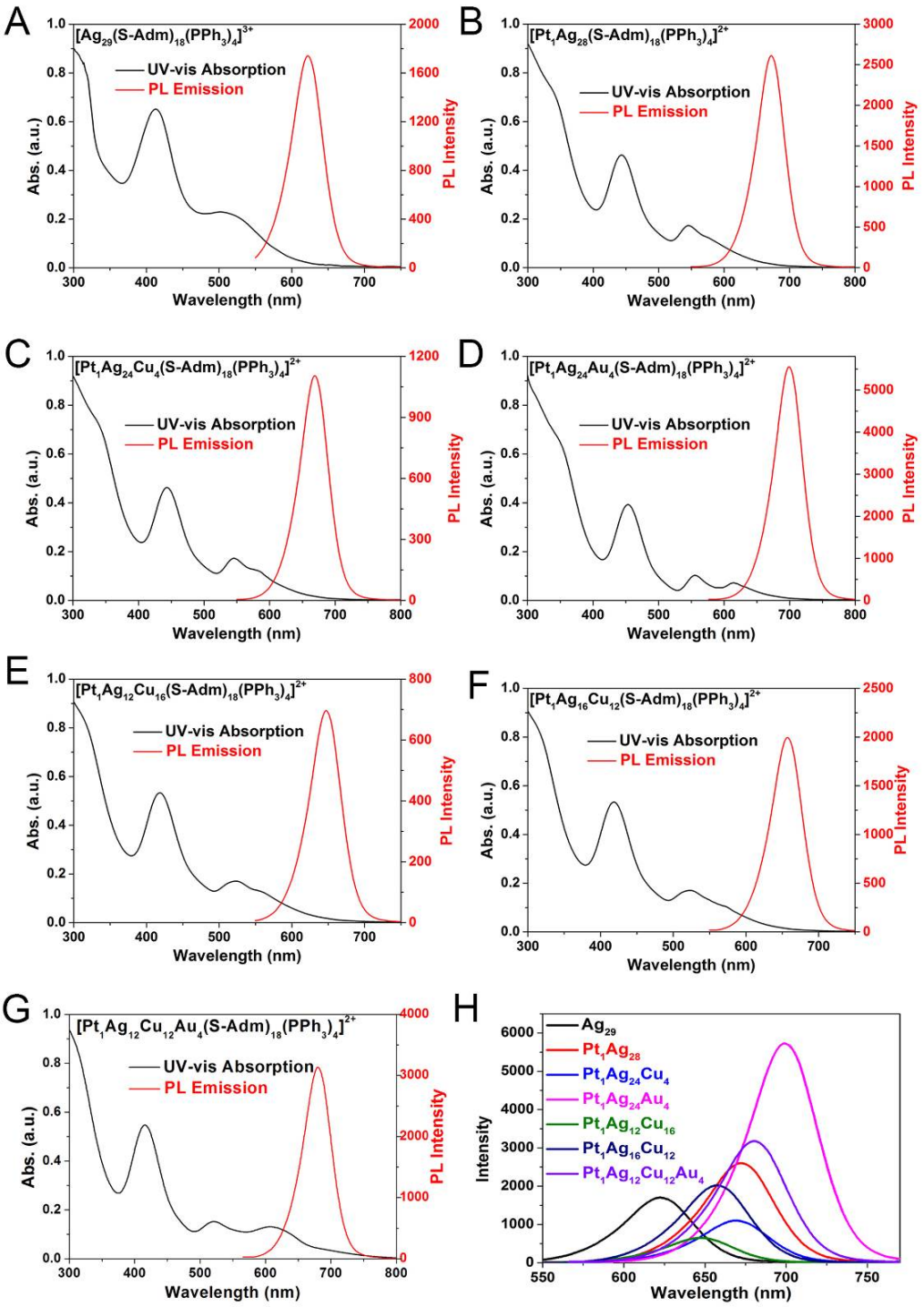

Fig. S41 UV-vis absorption and PL spectra of (A) mono-metallic Ag_{29}, (B) bi-metallic Pt_1Ag_{28}, (C) tri-metallic $Pt_1Ag_{24}Cu_4$, (D) tri-metallic $Pt_1Ag_{24}Au_4$, (E) tri-metallic $Pt_1Ag_{12}Cu_{16}$, (F) tri-metallic $Pt_1Ag_{16}Cu_{12}$, and (G) tetra-metallic $Pt_1Ag_{12}Cu_{12}Au_4$ nanoclusters. (H) Comparison of the PL wavelength and intensity of each nanocluster in the Pt-centered M_{29} nanosystem.

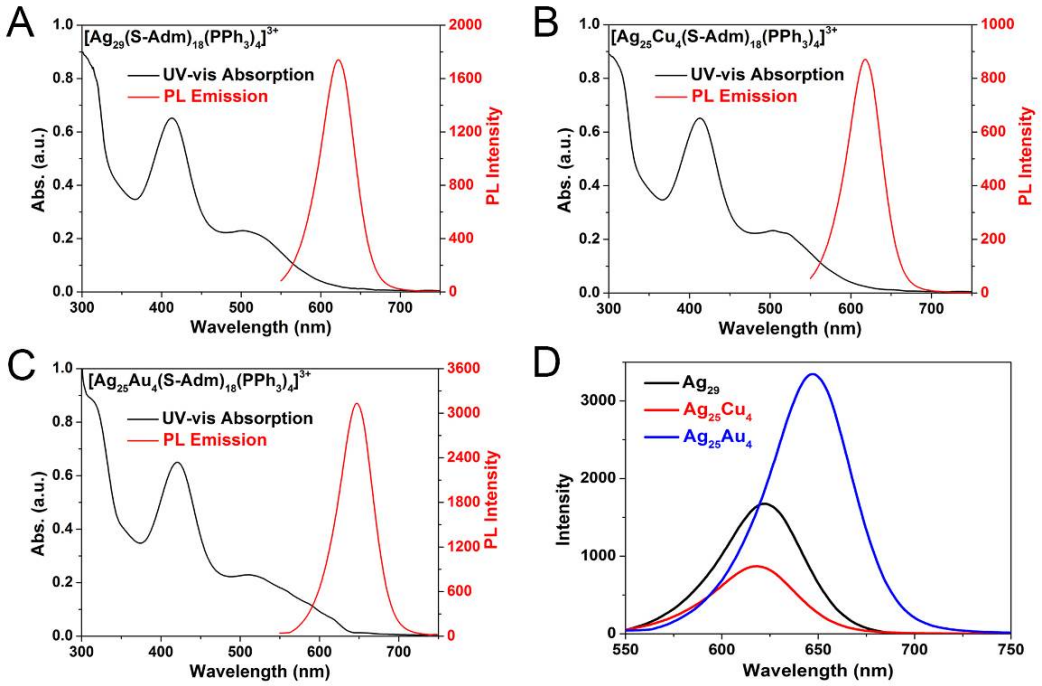

Fig. S42 UV-vis absorption and the PL spectra of (A) $[Ag_{29}(S\text{-}Adm)_{18}(PPh_3)_4]^{3+}$, (B) $[Ag_{25}Cu_4(S\text{-}Adm)_{18}(PPh_3)_4]^{3+}$, and (C) $[Ag_{25}Au_4(S\text{-}Adm)_{18}(PPh_3)_4]^{3+}$. (D) Comparison of the emission wavelength and intensity of each nanocluster in the Ag-centered M_{29} nanosystem.

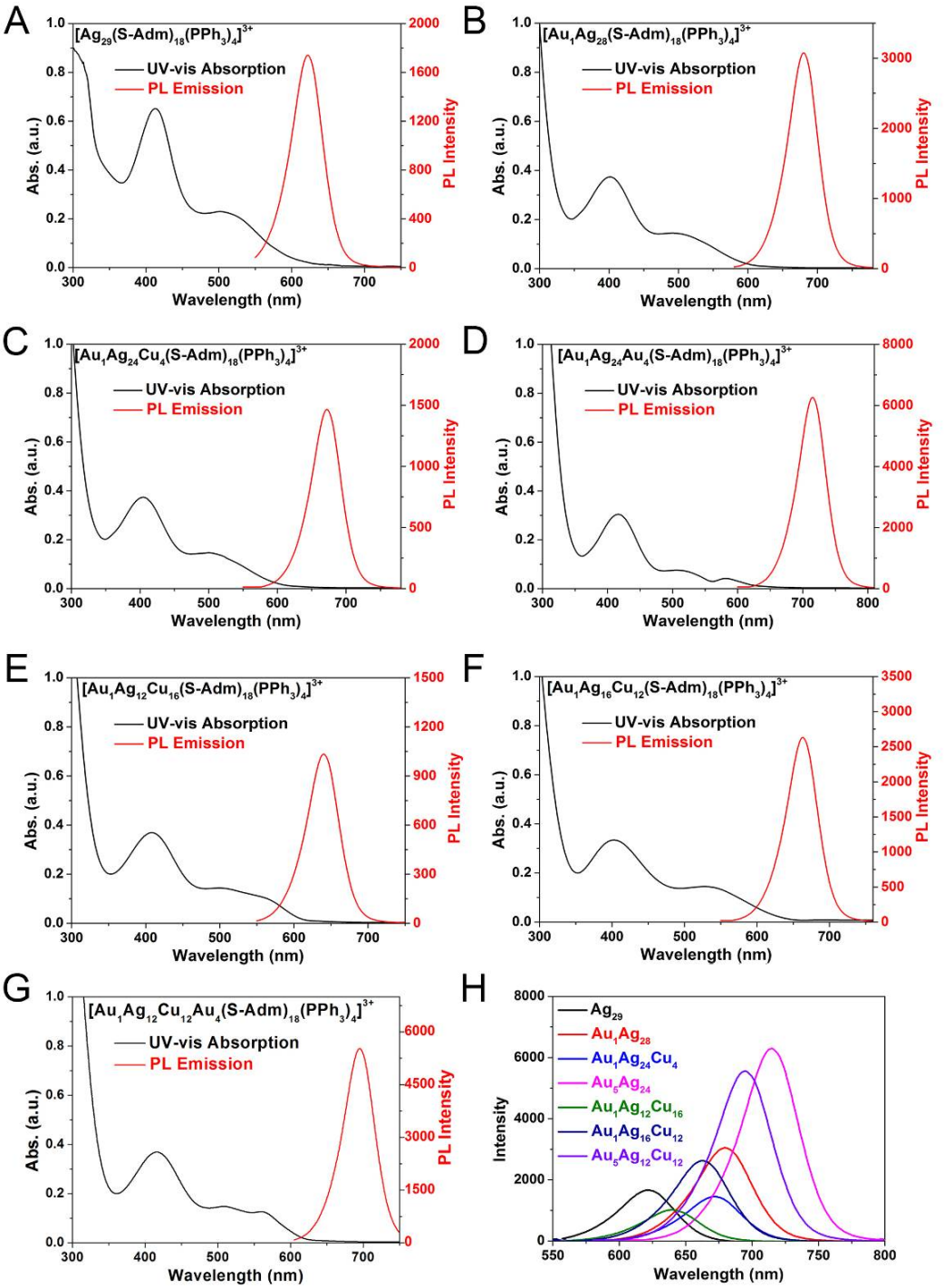

Fig. S43 UV-vis absorption and the PL spectra of (A) $[Ag_{29}(S\text{-}Adm)_{18}(PPh_3)_4]^{3+}$, (B) $[Au_1Ag_{28}(S\text{-}Adm)_{18}(PPh_3)_4]^{3+}$, (C) $[Au_1Ag_{24}Cu_4(S\text{-}Adm)_{18}(PPh_3)_4]^{3+}$, (D) $[Au_5Ag_{24}(S\text{-}Adm)_{18}(PPh_3)_4]^{3+}$, (E) $[Au_1Ag_{12}Cu_{16}(S\text{-}Adm)_{18}(PPh_3)_4]^{3+}$, (F) $[Au_1Ag_{16}Cu_{12}(S\text{-}Adm)_{18}(PPh_3)_4]^{3+}$ and (G) $[Au_5Ag_{12}Cu_{12}(S\text{-}Adm)_{18}(PPh_3)_4]^{3+}$ nanoclusters. (H) Comparison of the emission wavelength and intensity of each nanocluster in the Au-centered M_{29} nanosystem.

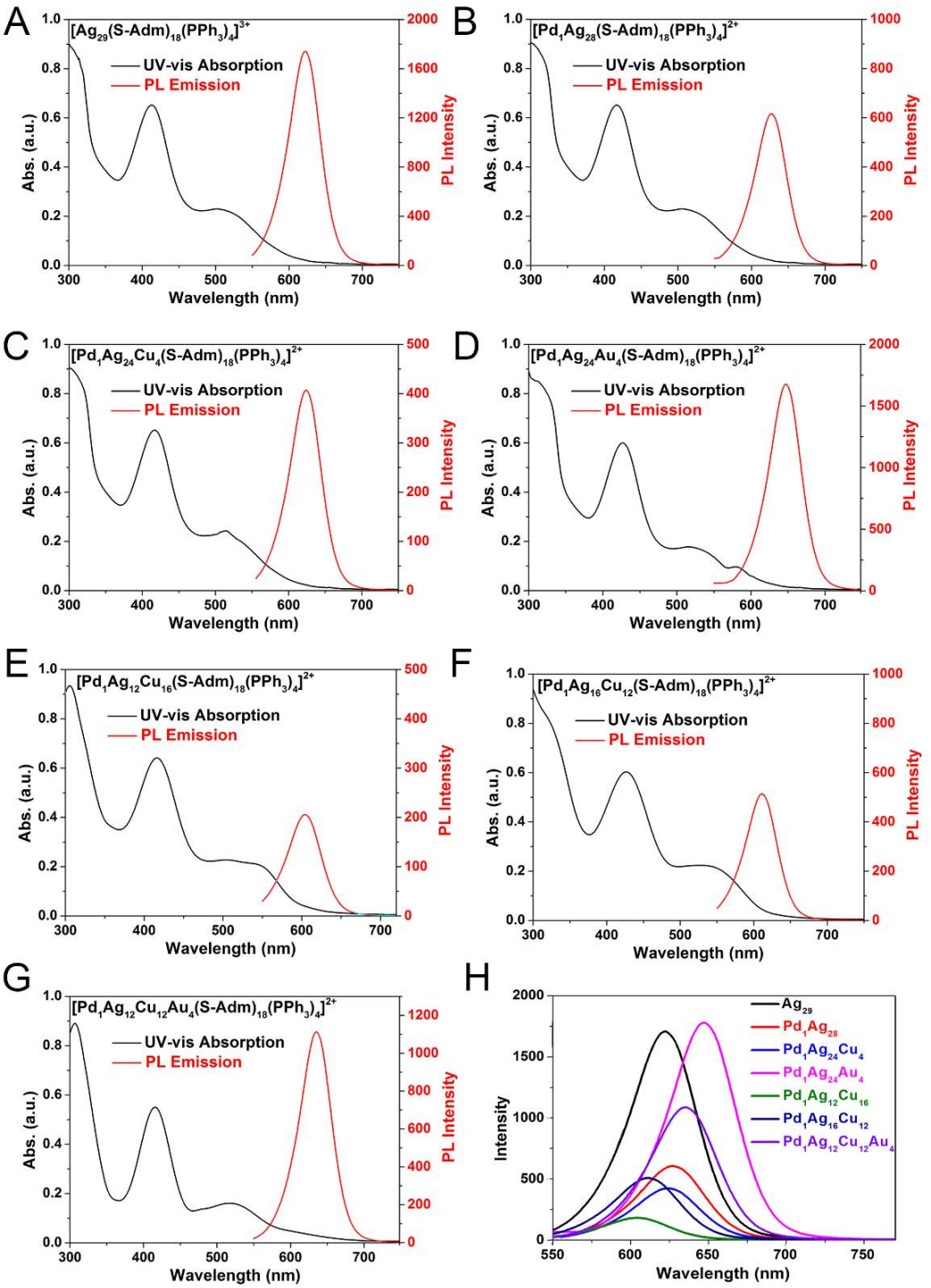

Fig. S44 UV-vis absorption and the PL spectra of (A) $[Ag_{29}(S\text{-}Adm)_{18}(PPh_3)_4]^{3+}$, (B) $[Pd_1Ag_{28}(S\text{-}Adm)_{18}(PPh_3)_4]^{2+}$, (C) $[Pd_1Ag_{24}Cu_4(S\text{-}Adm)_{18}(PPh_3)_4]^{2+}$, (D) $[Pd_1Ag_{24}Au_4(S\text{-}Adm)_{18}(PPh_3)_4]^{2+}$, (E) $[Pd_1Ag_{12}Cu_{16}(S\text{-}Adm)_{18}(PPh_3)_4]^{2+}$, (F) $[Pd_1Ag_{16}Cu_{12}(S\text{-}Adm)_{18}(PPh_3)_4]^{2+}$, and (G) $[Pd_1Ag_{12}Cu_{12}Au_4(S\text{-}Adm)_{18}(PPh_3)_4]^{2+}$ nanoclusters. (H) Comparison of the emission wavelength and intensity of each nanocluster in the Pd-centered M_{29} nanosystem.

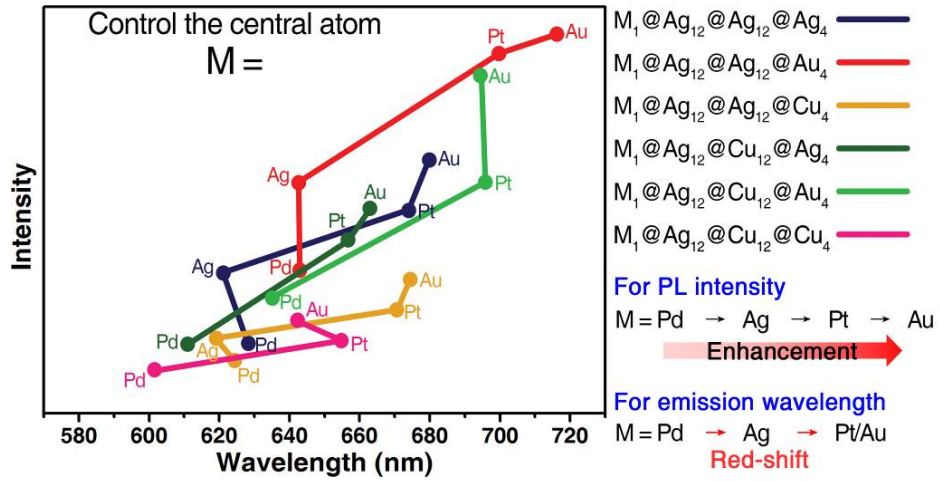

Fig. 45 Correlations between the central atom and PL property of the M_{29} system.

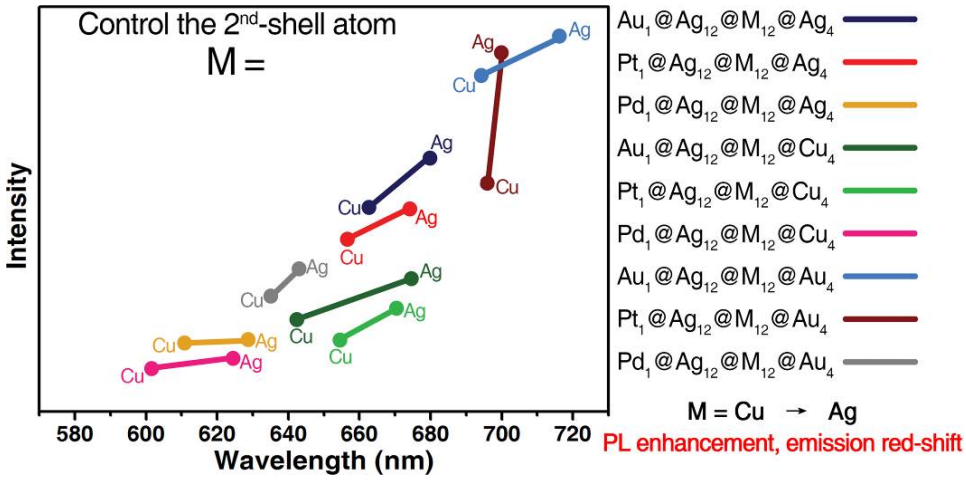

Fig. S46 Correlations between the 2nd-shell atom and PL property of the M_{29} system.

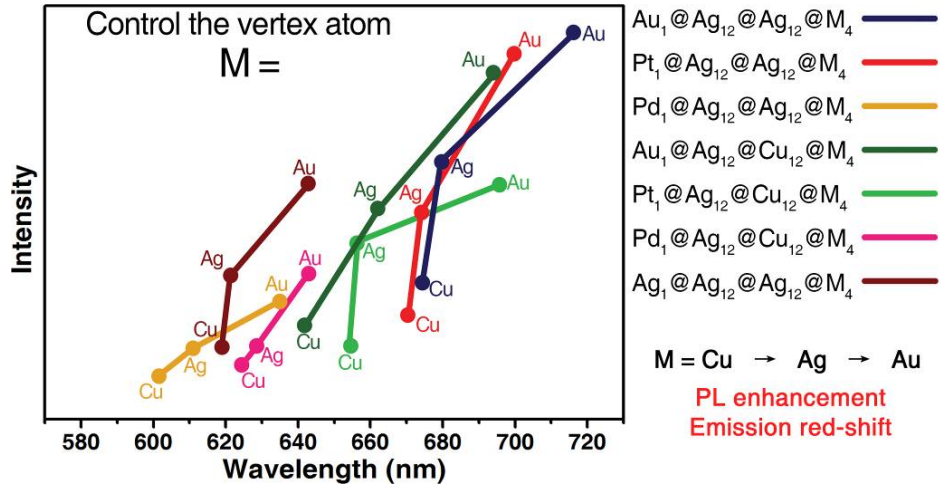

Fig. S47 Correlations between the vertex atom and PL property of the M_{29} system.

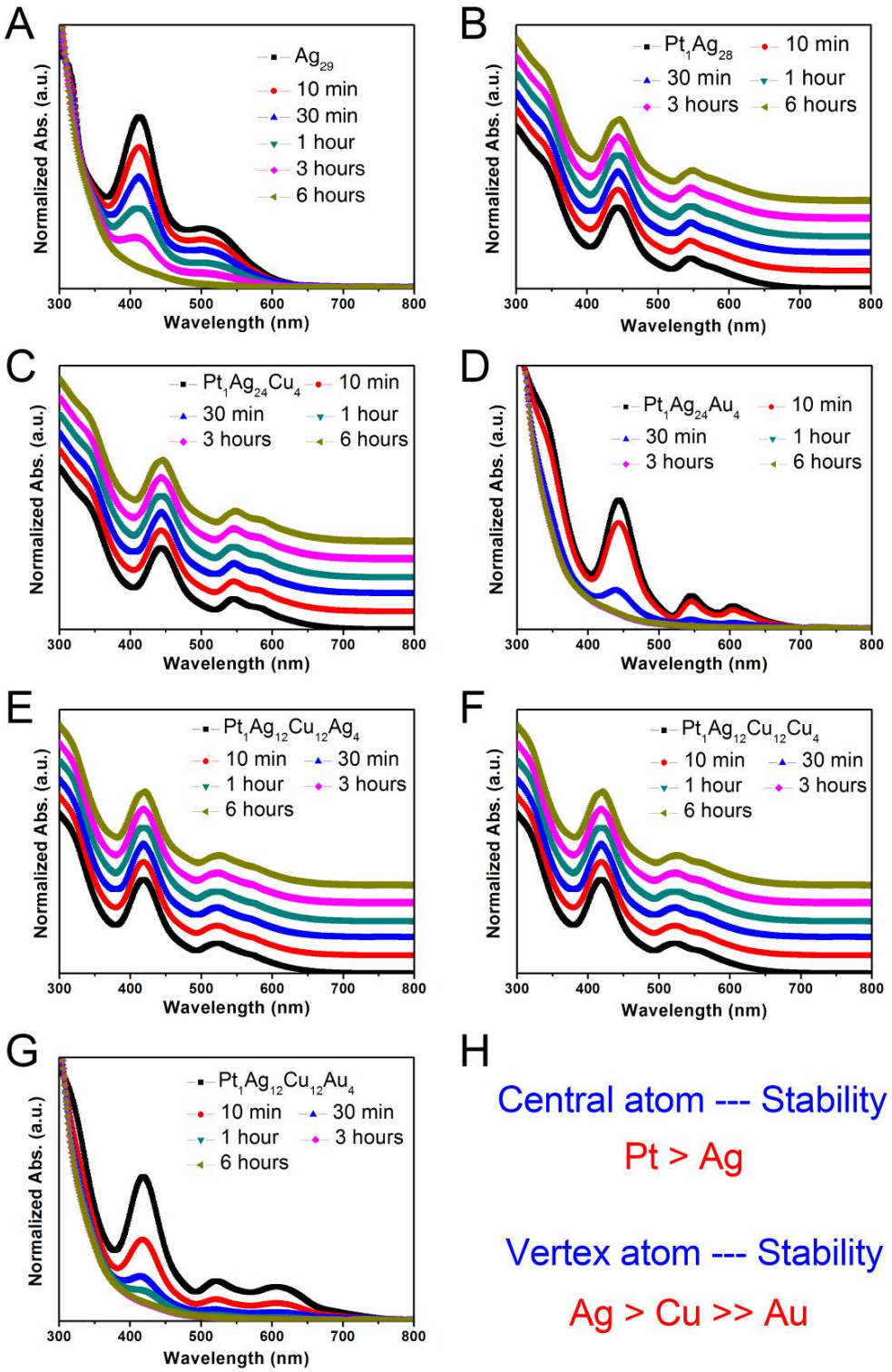

Fig. S48 Stability test of (A) mono-metallic Ag_{29}, (B) bi-metallic Pt_1Ag_{28}, (C) tri-metallic $Pt_1Ag_{24}Cu_4$, (D) tri-metallic $Pt_1Ag_{24}Au_4$, (E) tri-metallic $Pt_1Ag_{12}Cu_{16}$, (F) tri-metallic $Pt_1Ag_{16}Cu_{12}$, and (G) tetra-metallic $Pt_1Ag_{12}Cu_{12}Au_4$ nanoclusters at room temperature. (H) Correlations between the central atom or the vertex atom and the stability of M_{29} nanoclusters.

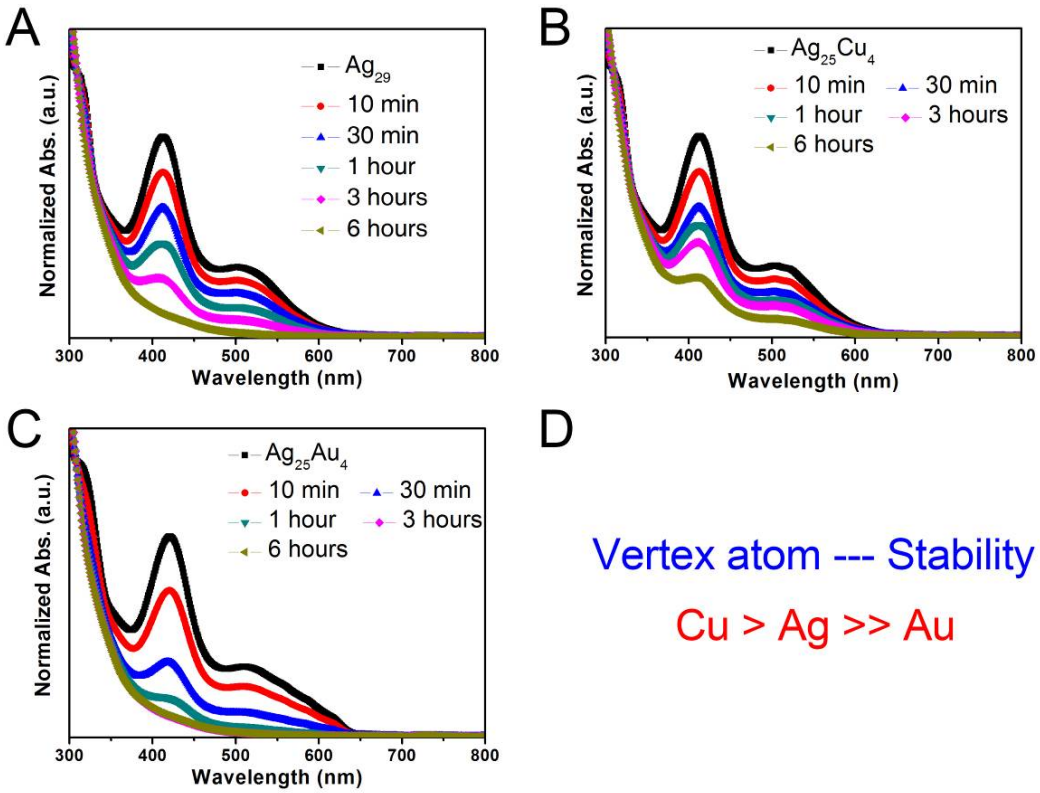

Fig. S49 Stability test of (A) $[Ag_{29}(S\text{-}Adm)_{18}(PPh_3)_4]^{3+}$, (B) $[Ag_{25}Cu_4(S\text{-}Adm)_{18}(PPh_3)_4]^{3+}$, and (C) $[Ag_{25}Au_4(S\text{-}Adm)_{18}(PPh_3)_4]^{3+}$ nanoclusters at room temperature. (D) (H) Correlations between the vertex atom and the stability of M_{29} nanoclusters.

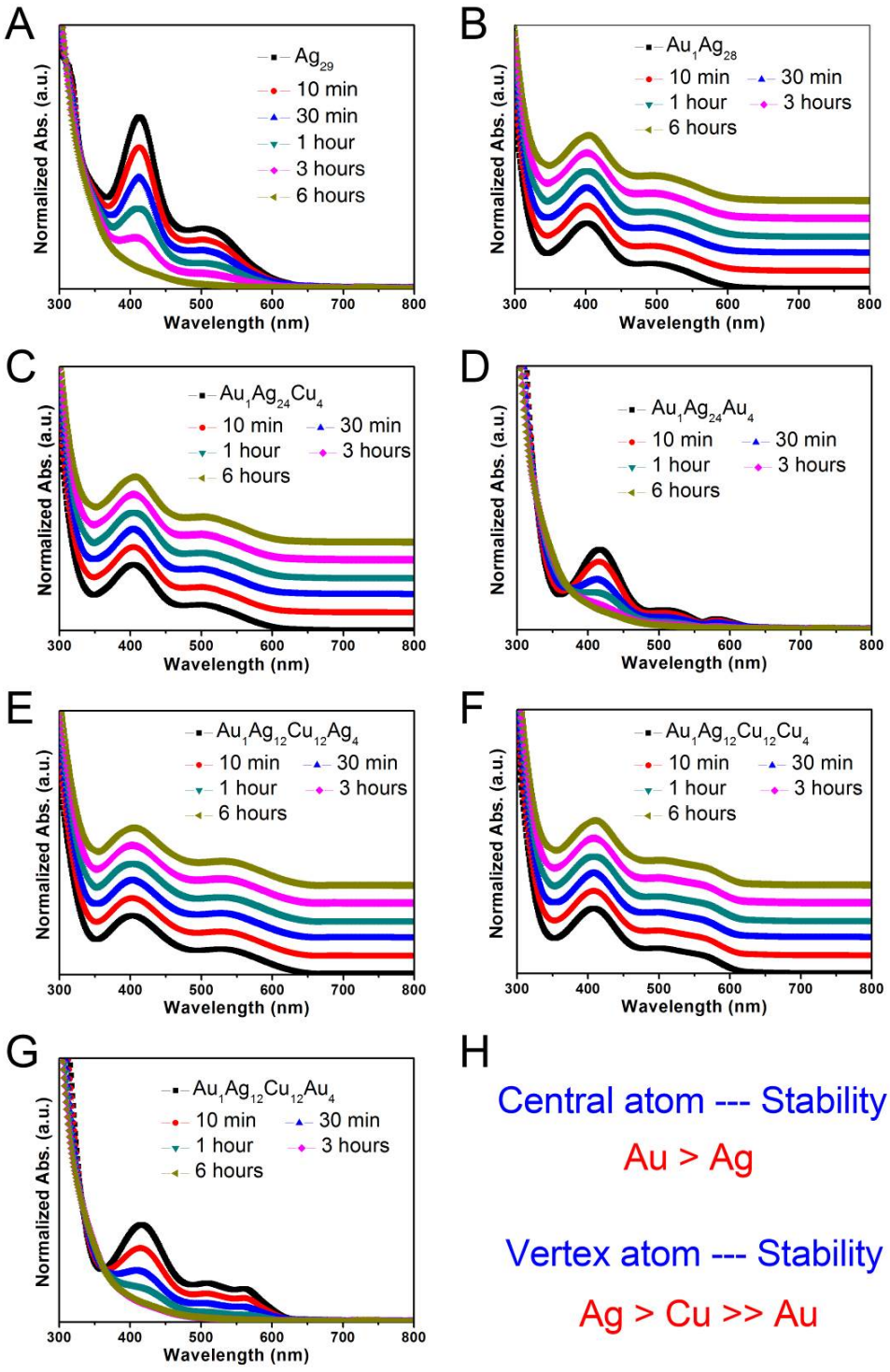

Fig. S50 Stability of (A) $[Ag_{29}(S\text{-}Adm)_{18}(PPh_3)_4]^{3+}$, (B) $[Au_1Ag_{28}(S\text{-}Adm)_{18}(PPh_3)_4]^{3+}$, (C) $[Au_1Ag_{24}Cu_4(S\text{-}Adm)_{18}(PPh_3)_4]^{3+}$, (D) $[Au_5Ag_{24}(S\text{-}Adm)_{18}(PPh_3)_4]^{3+}$, (E) $[Au_1Ag_{12}Cu_{16}(S\text{-}Adm)_{18}(PPh_3)_4]^{3+}$, (F) $[Au_1Ag_{16}Cu_{12}(S\text{-}Adm)_{18}(PPh_3)_4]^{3+}$ and (G) $[Au_5Ag_{12}Cu_{12}(S\text{-}Adm)_{18}(PPh_3)_4]^{3+}$ nanoclusters at room temperature. (H) Correlations between the central atom or the vertex atom and the stability of M_{29} nanoclusters.

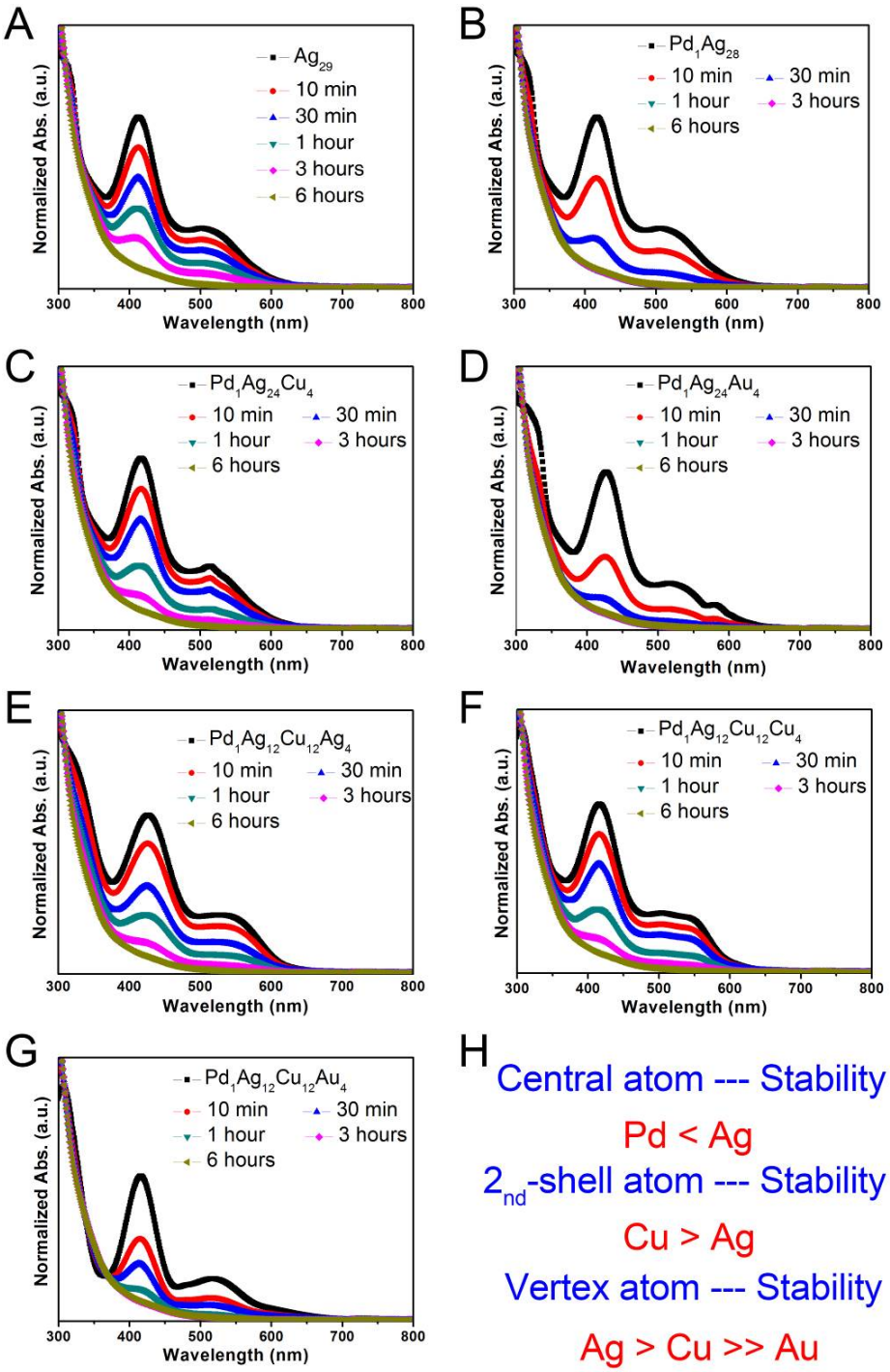

Fig. S51 Stability of (A) $[Ag_{29}(S\text{-}Adm)_{18}(PPh_3)_4]^{3+}$, (B) $[Pd_1Ag_{28}(S\text{-}Adm)_{18}(PPh_3)_4]^{2+}$, (C) $[Pd_1Ag_{24}Cu_4(S\text{-}Adm)_{18}(PPh_3)_4]^{2+}$, (D) $[Pd_1Ag_{24}Au_4(S\text{-}Adm)_{18}(PPh_3)_4]^{2+}$, (E) $[Pd_1Ag_{12}Cu_{16}(S\text{-}Adm)_{18}(PPh_3)_4]^{2+}$, (F) $[Pd_1Ag_{16}Cu_{12}(S\text{-}Adm)_{18}(PPh_3)_4]^{2+}$, and (G) $[Pd_1Ag_{12}Cu_{12}Au_4(S\text{-}Adm)_{18}(PPh_3)_4]^{2+}$ nanoclusters at room temperature. (H) Correlations between the central atom or the vertex atom and the stability of M_{29} nanoclusters.

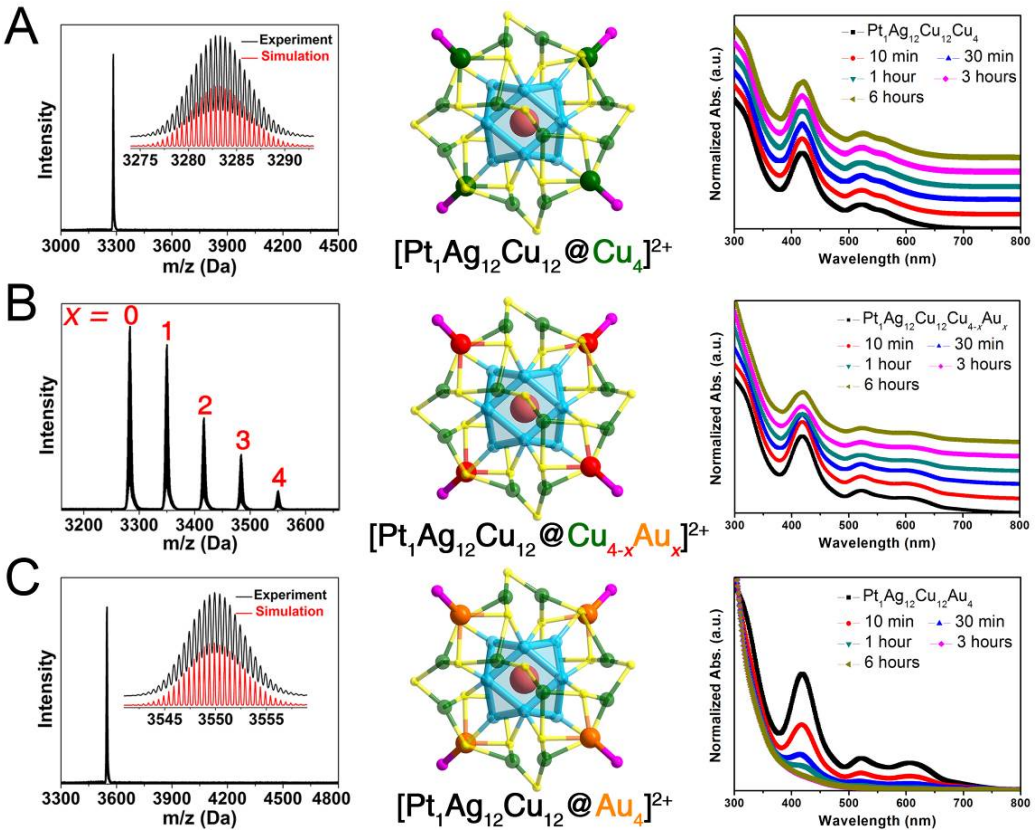

Fig. S52 Stability of (A) $[Pt_1Ag_{12}Cu_{12}Cu_4(S\text{-}Adm)_{18}(PPh_3)_4]^{2+}$, (B) $[Pt_1Ag_{12}Cu_{12}Cu_{4-x}Au_x(S\text{-}Adm)_{18}(PPh_3)_4]^{2+}$, and (C) $[Pt_1Ag_{12}Cu_{12}Au_4(S\text{-}Adm)_{18}(PPh_3)_4]^{2+}$ at room temperature.

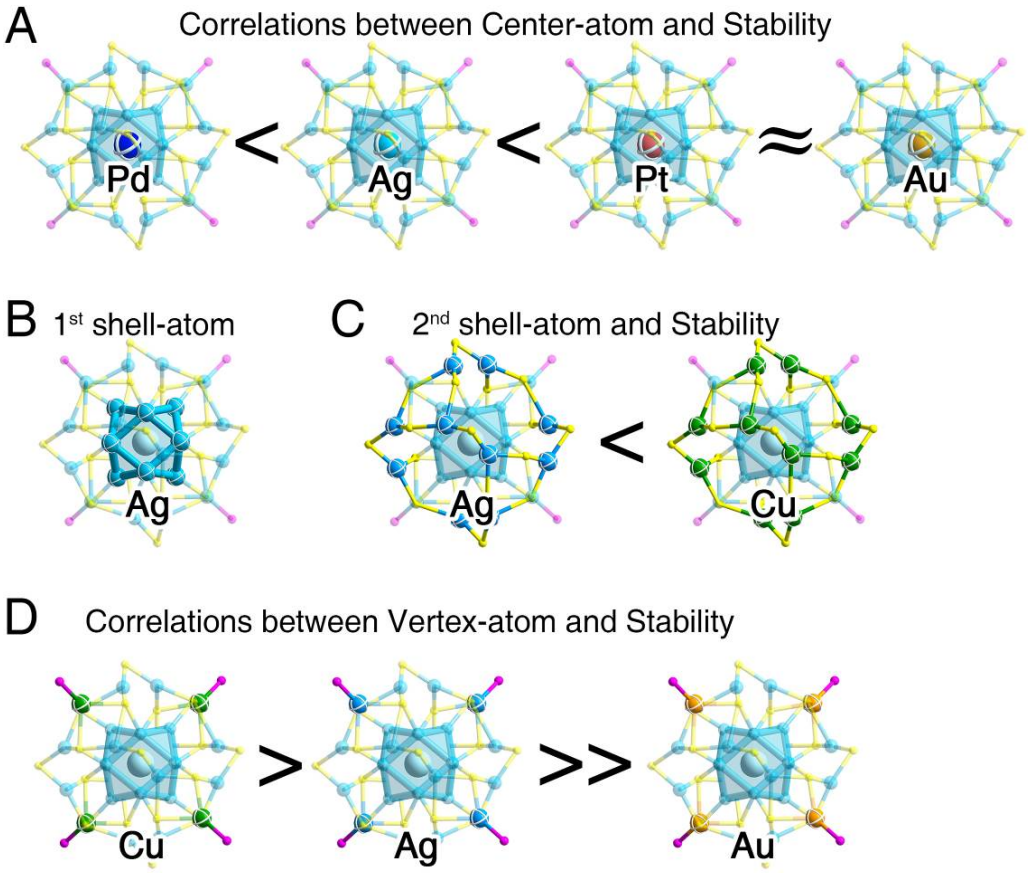

Fig. S53 Illustrations of the way to enhance the stability of the M_{29} nanocluster.

Table S1. Elemental analysis (EA) results of the M_{29} (M = Ag/Au/Pt/Pd/Cu) nanoclusters.

Sample	Elemental Analysis	
	Cal.	Exp.
$Ag_{29}(SR)_{18}(PPh_3)_4$	C: 42.11%; H: 4.63%	C: 42.14%; H: 4.66%
$Ag_{25}Cu_4(SR)_{18}(PPh_3)_4$	C: 43.17%; H: 4.74%	C: 43.22%; H: 4.74%
$Pt_1Ag_{28}(SR)_{18}(PPh_3)_4$	C: 41.60%; H: 4.57%	C: 41.60%; H: 4.59%
$Pt_1Ag_{24}Cu_4(SR)_{18}(PPh_3)_4$	C: 42.64%; H: 4.69%	C: 42.69%; H: 4.72%
$Pt_1Ag_{12}Cu_{16}(SR)_{18}(PPh_3)_4$	C: 46.09%; H: 5.07%	C: 46.13%; H: 5.13%
$Pt_1Ag_{16}Cu_{12}(SR)_{18}(PPh_3)_4$	C: 44.89%; H: 4.93%	C: 44.81%; H: 4.93%
$Au_1Ag_{28}(SR)_{18}(PPh_3)_4$	C: 41.59%; H: 4.57%	C: 41.59%; H: 4.44%
$Au_1Ag_{24}Cu_4(SR)_{18}(PPh_3)_4$	C: 42.63%; H: 4.68%	C: 42.61%; H: 4.64%
$Au_1Ag_{12}Cu_{16}(SR)_{18}(PPh_3)_4$	C: 46.08%; H: 5.06%	C: 46.08%; H: 5.22%
$Au_1Ag_{16}Cu_{12}(SR)_{18}(PPh_3)_4$	C: 44.87%; H: 4.93%	C: 44.89%; H: 5.01%
$Pd_1Ag_{28}(SR)_{18}(PPh_3)_4$	C: 42.11%; H: 4.63%	C: 42.13%; H: 4.66%
$Pd_1Ag_{24}Cu_4(SR)_{18}(PPh_3)_4$	C: 43.18%; H: 4.74%	C: 43.18%; H: 4.77%
$Pd_1Ag_{12}Cu_{16}(SR)_{18}(PPh_3)_4$	C: 46.73%; H: 5.13%	C: 46.71%; H: 5.11%
$Pd_1Ag_{16}Cu_{12}(SR)_{18}(PPh_3)_4$	C: 45.48%; H: 5.07%	C: 45.44%; H: 5.07%

Table S2. Inductively coupled plasma-atomic emission spectrometry (ICP-AES) results of the M_{29} (M = Ag/Au/Pt/Pd/Cu) nanoclusters.

Sample	ICP-AES analysis	
	Cal.	Exp.
$Ag_{25}Cu_4(SR)_{18}(PPh_3)_4$	Ag: 86.21%; Cu: 13.79%	Ag: 85.89%; Cu: 14.11%
$Pt_1Ag_{28}(SR)_{18}(PPh_3)_4$	Pt: 3.45%; Ag: 96.55%	Pt: 3.27%; Ag: 96.73%
$Pt_1Ag_{24}Cu_4(SR)_{18}(PPh_3)_4$	Pt: 3.45%; Ag: 82.76%; Cu: 13.79%	Pt: 3.11%; Ag: 83.45%; Cu: 13.44%
$Pt_1Ag_{12}Cu_{16}(SR)_{18}(PPh_3)_4$	Pt: 3.45%; Ag: 41.38%; Cu: 55.17%	Pt: 3.63%; Ag: 40.51%; Cu: 55.86%
$Pt_1Ag_{16}Cu_{12}(SR)_{18}(PPh_3)_4$	Pt: 3.45%; Ag: 55.17%; Cu: 41.39%	Pt: 3.41%; Ag: 56.02 %; Cu: 40.57%
$Au_1Ag_{28}(SR)_{18}(PPh_3)_4$	Au: 3.45%; Ag: 96.55%	Au: 3.51%; Ag: 96.49%
$Au_1Ag_{24}Cu_4(SR)_{18}(PPh_3)_4$	Au: 3.45%; Ag: 82.76%; Cu: 13.79%	Au: 3.62%; Ag: 82.01%; Cu: 14.37%
$Au_1Ag_{12}Cu_{16}(SR)_{18}(PPh_3)_4$	Au: 3.45%; Ag: 41.38%; Cu: 55.17%	Au: 3.28%; Ag: 40.94%; Cu: 55.78%
$Au_1Ag_{16}Cu_{12}(SR)_{18}(PPh_3)_4$	Au: 3.45%; Ag: 55.17%; Cu: 41.39%	Au: 3.49%; Ag: 55.82%; Cu: 40.69%
$Pd_1Ag_{28}(SR)_{18}(PPh_3)_4$	Pd: 3.45%; Ag: 96.55%	Pd: 3.29%; Ag: 96.71%
$Pd_1Ag_{24}Cu_4(SR)_{18}(PPh_3)_4$	Pd: 3.45%; Ag: 82.76%; Cu: 13.79%	Pd: 3.22%; Ag: 83.42%; Cu: 13.36%
$Pd_1Ag_{12}Cu_{16}(SR)_{18}(PPh_3)_4$	Pd: 3.45%; Ag: 41.38%; Cu: 55.17%	Pd: 3.37%; Ag: 41.70%; Cu: 54.93%
$Pd_1Ag_{16}Cu_{12}(SR)_{18}(PPh_3)_4$	Pd: 3.45%; Ag: 55.17%; Cu: 41.39%	Pd: 3.64%; Ag: 55.92%; Cu: 40.44%

Table S3. Crystal data and structure refinement for $Au_1Ag_{28}(S\text{-}Adm)_{18}(PPh_3)_4$ nanocluster (CCDC: 1872544).

Identification code	$Au_1Ag_{28}(S\text{-}Adm)_{18}(PPh_3)_4$
Empirical formula	C255H311Ag28AuP4S182(C24H18B)
Formula weight	8442.28
Temperature/K	180
Crystal system	monoclinic
Space group	I 1 2/a 1
a/Å	37.149(3)
b/Å	25.0838(18)
c/Å	37.150(3)
α/°	90
β/°	92.318(7)
γ/°	90
Volume/$Å^3$	34589(5)
Z	4
$\rho_{calc}g/cm^3$	1.621
μ/mm^{-1}	2.231
F(000)	16696
Crystal size/mm^3	0.1 × 0.1 × 0.1
Radiation	MoKα (λ = 0.71073)
Index ranges	$-44 \le h \le 44$, $-29 \le k \le 29$, $-44 \le l \le 44$
Final R indexes [I>=2σ (I)]	$R_1 = 0.1355$, $wR_2 = 0.3047$
Final R indexes [all data]	$R_1 = 0.2300$, $wR_2 = 0.3492$

Table S4. Crystal data and structure refinement for $Pt_1Ag_{12}Cu_{16}(S\text{-}Adm)_{18}(PPh_3)_4$ nanocluster (CCDC: 1872534).

Identification code	$Pt_1Ag_{12}Cu_{16}(S\text{-}Adm)_{18}(PPh_3)_4$
Empirical formula	C252H330Ag12Cu16P4PtS18
Formula weight	6566.27
Temperature/K	153
Crystal system	triclinic
Space group	P 1
a/Å	24.955(2)
b/Å	28.968(3)
c/Å	29.0160(16)
α/°	79.750(4)
β/°	65.563(3)
γ/°	64.557(3)
Volume/Å^3	17245(3)
Z	1
ρ_{calc}g/cm^3	0.632
μ/mm^{-1}	1.097
F(000)	3296
Crystal size/mm^3	0.220 × 0.200 × 0.180
Radiation	MoKα (λ = 0.71073)
Index ranges	-32 ≤ h ≤ 32, -37 ≤ k ≤ 37, -37 ≤ l ≤ 37
Final R indexes [I>=2σ (I)]	R_1 = 0.0501, wR_2 = 0.1042
Final R indexes [all data]	R_1 = 0.0512, wR_2 = 0.1044